Research Highlights

Probing a Horizontal Line Node in the Heavy-Fermion Superconductor URu_2Si_2 by Angle-Resolved Heat Capacity Measurements

Sakakibara Group

Identification of the gap structure of anisotropic superconductors (SCs) has been the subject of intensive study over many years. Among various experimental techniques, the heat capacity (C_ϕ) measurement in a rotating magnetic field (H) is quite useful because of its wide applicability. This technique is based on the fact that the field-induced zero-energy density of states, $N(E=0)$, in the superconducting mixed state of a nodal SC is field and its orientation dependent. In the case of a tetragonal SC with vertical line nodes, in particular, C_ϕ shows an angular oscillation when H is rotated in the basal plane, with C_ϕ minima occurring along the nodal directions.

To probe the horizontal line node, however, is not so easy. When H is rotated in the *ac* plane of the tetragonal crystal, the polar angle (θ) variation of the heat capacity $C_\theta(H)$ is expected to exhibit a twofold oscillation reflecting the gap structure. It should be reminded, however, that because of the tetragonal symmetry of the lattice, the upper critical field H_{c2} would have a substantial twofold anisotropy in the *ac* plane and give rise to a strong twofold background in $C_\theta(H)$. Hence, the simple argument—the direction of minima in $C_\theta(H)$ corresponds to the nodal direction—does not hold.

Nevertheless, because the θ variation of the field-induced $N(E=0)$ would exhibit local minima as the direction of H passes through the horizontal line node, fine structures may appear in the twofold oscillation of $C_\theta(H)$. We applied this technique to the heavy fermion superconductor URu_2Si_2 [1], whose gap structure is suggested by previous experiments to be a chiral *d*-wave, $k_z(k_x+ik_y)$, having a horizontal line node and polar point nodes [2,3].

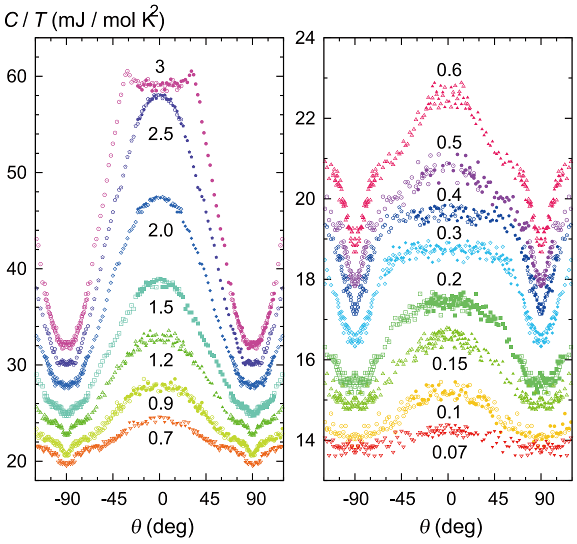

Fig. 1. Polar angle dependence of C/T of URu_2Si_2 measured at 0.2 K in various magnetic fields ranging from 0.07 to 3 T.

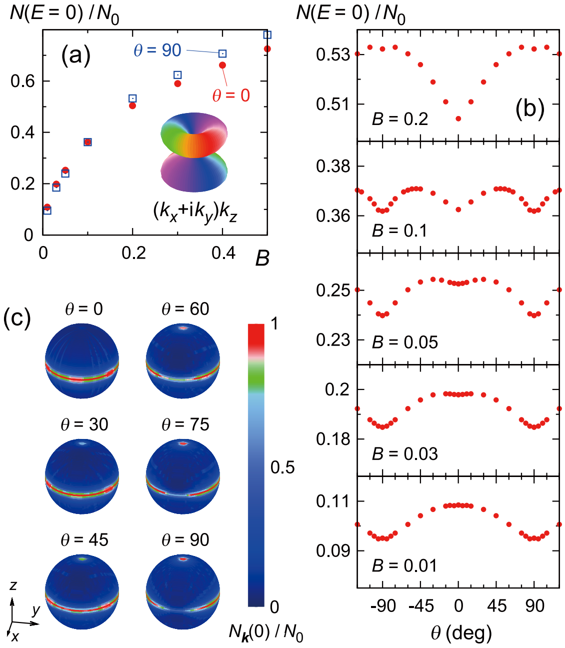

Fig. 2. (a) Field dependence of $N(E=0)$ for $B \| z$ and $B \| x$, obtained by microscopic calculations assuming the $k_z(k_x+ik_y)$ gap. (b) Calculated polar angle variation of $N(E=0)$ at several fields. (c) Angle-resolved density of states, $N_k(0)$, mapped on the spherical Fermi surface. The magnetic field is rotated in the *xz* plane.

Figure 1 shows the measured results of $C_\theta(H)$ obtained by rotating H within the *ac* plane. At high fields, the large twofold oscillation is observed, reflecting the anisotropy of H_{c2} predominantly due to the anisotropic Pauli paramagnetic effect. In the low-field region below 0.15 T, no remarkable anomaly was detected in $C(\theta)$: the data can be fitted by a simple twofold function expected for an effective mass model. By contrast, a striking feature is found in $C(\theta)$ in the region 0.2~1.5 T; a shoulder-like anomaly appears at around θ~45º. With increasing H, this anomaly slightly moves to the higher θ side.

We calculate the θ dependence of the $N(E=0)$ on the basis of the microscopic Eilenberger theory assuming the gap symmetry of $k_z(k_x+ik_y)$ [inset of Fig. 2(a)] and a single-band spherical Fermi surface. For simplicity, the Pauli-paramagnetic effect and the anisotropy of the Fermi velocity are not taken into account. Figure 2(a) shows the field dependence of $N(E=0)$ at θ=0 ($H \| z$) and 90º. For both field directions, $H^{1/2}$ dependence is obtained reflecting the line node. Note that a small anisotropy appears in $N(E = 0)$.

In Fig. 2(b), $N(E=0)$ is plotted as a function of θ at several fields. The calculated result at a low field $B=0.03$ can reproduce the features observed in the present experiment, i.e. the shoulder-like anomaly and the dip structure in $C(\theta)$ observed at moderate fields. With increasing B, a sharp dip develops at θ=0 and then the anisotropy in $N(E=0)$ is reversed above $B \sim 0.1$, reflecting the H_{c2} anisotropy. The dip at θ=0 and the reversal of the $C(\theta)$ anisotropy in the high-field region, demonstrated in Fig. 2(b), were not detected in the experiment because the actual H_{c2} anisotropy depends on the strong Pauli-paramagnetic effect. Figure 2(c) shows the momentum-resolved density of states, $N_k(0)$, mapped on the spherical Fermi surface. The field B=0.03 is rotated in the xz plane. When $B \| z$ (θ=0), strong quasiparticle excitations occur on the line node as indicated by a red color. As B rotates towards x direction, the quasiparticle excitations at the region k_y=0 are strongly reduced, resulting in a decrease in $N(E=0)$. This effects account the shoulder-like feature in $C(\theta)$ near 45°.

The present results indicate that a horizontal line node exists in URu_2Si_2. Note that among the possible gap structures for a tetragonal even parity SC, only $k_z(k_x+ik_y)$ has the horizontal line node. Thus, the pairing symmetry of URu_2Si_2 is likely to be the chiral d wave [1].

References
[1] S. Kittaka *et al*., J. Phys. Soc. Jpn. **85**, 033704 (2016).
[2] Y. Kasahara, T. Iwasawa, H. Shishido, T. Shibauchi, K. Behnia, Y. Haga, T. D. Matsuda, Y. Onuki, M. Siglist, and Y. Matsuda, Phys. Rev. Lett. **99**, 116402 (2007).
[3] K. Yano, T. Sakakibara, T. Tayama, M. Yokoyama, H. Amitsuka, Y. Homma, P. Miranović, M. Ichioka, Y. Tsutsumi, and K. Machida, Phys. Rev. Lett. **100**, 017004 (2008).

Authors
S. Kittaka, Y. Shimizu, T. Sakakibara, Y. Haga[a], E. Yamamoto[a], Y. Onuki[a,b], Y. Tsutsumi[c,d], T. Nomoto[e], H. Ikeda[f], K. Machida[f]
[a]JAEA
[b]University of Ryukyu
[c]University of Tokyo
[d]RIKEN
[e]Kyoto University
[f]Ritsumeikan University

Solid-Solid Interconversion Coupled by Jahn-Teller-Like Distortion and Bond-Order for the Hydrogen-Bonded Molecular Conductor β'-[H_3(Cat-EDO-TTF)$_2$]BF_4

Mori Group

In the field of molecular functional materials, "π-electronic properties" of (super)conductors and anti/ferromagnets and "protonic properties" of anti/ferro-electrics and proton conductor have been investigated separately and independently. Our aim is to couple "π-electronic properties" and "protonic properties" and to create novel "proton and π-electron coupled (PEC) properties and functionalities". Recently, in the catechol-fused tetrathiafulvalene (TTF) system [1], the metallic state of purely organic single-unit crystal of κ-H_3(Cat-EDT-ST)$_2$ [2], the quantum spin liquid state of κ-H_3(Cat-EDT-TTF)$_2$ [3], and electronic switching induced by deuterium and charge transfer of κ-D_3(Cat-EDT-TTF)$_2$ and κ-D_3(Cat-EDT-ST)$_2$ [4,5] have been unveiled. Here we report unprecedented solid-solid interconversion coupled by Jahn-Teller-like distortion of hydrogen-bond (H-bond) unit and bond-order for the molecular conductor β'-[H_3(Cat-EDO-TTF)$_2$]BF_4 [6].

The present crystal is composed of an H-bonded unit structure [H_3(Cat-EDO-TTF)$_2$]$^+$ and an additional BF_4^- anion (positionally disordered), to give a chemical formula of [H_3(Cat-EDO-TTF)$_2$]BF_4. In addition, this H-bond unit, [H_3(Cat-EDO-TTF)$_2$]$^+$, is highly planar, and the H-bond part has an anionic symmetric [O..H..O]$^-$ structure with a short O..O distance (2.455(3) Å), whose H-bonded hydrogen occupies the inversion center of the H-bonded unit. Thus, two Cat-EDO-TTF skeletons in the unit are crystallographically equivalent to each other (Fig. 1). In the present EDO-TTF is +1 state, as estimated from empirical bond length analysis of the TTF skeleton due to the inclusion of the BF_4^- anion in the present system to maintain the charge neutrality of the overall crystal. As a result, the EDO-TFF system is expected to have a larger charge polarization within the H-bonded unit, [(EDO-TTF$^+$-Cat)-[O..H..O]$^-$-(Cat-TTF$^+$-EDO)]$^+$ The present planar H-bonded molecular units form a sheet-like structure including the BF_4^- anions, which is further stacked to construct a so-called β'-type two-dimensional conducting layer composed of Cat-EDOTTF$^+$ molecules. Thus, the high temperature phase (HTP: high temperature phase, 220 K < T) crystal can be called β'-[H_3(Cat-EDO-TTF)$_2$]BF_4. As shown by red dashed circles in Fig. 1, the Cat-EDO-TTF$^+$ molecules are π-dimerized in a head-to-tail manner with an interplanar distance of 3.41 Å, which is much shorter than that between the π-dimers (3.60 Å). Actually, the calculated transfer integral within the π-dimer (134 meV, denoted by

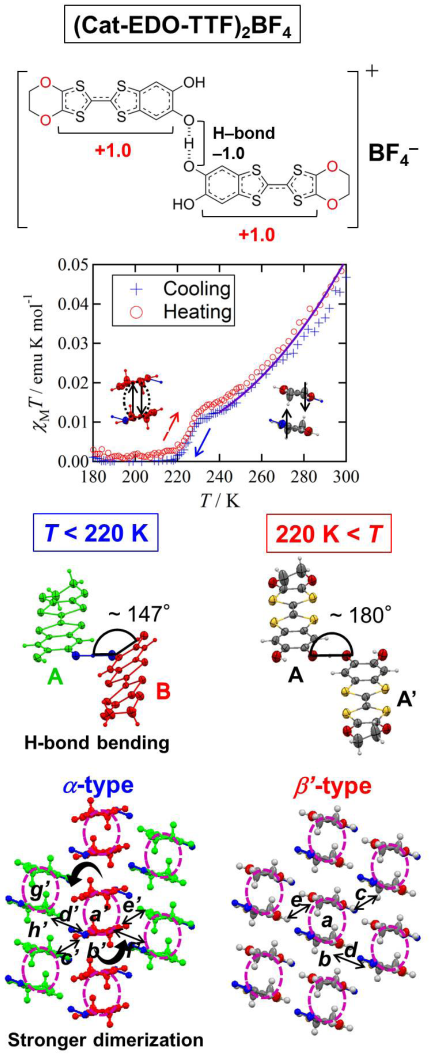

Fig. 1. The solid-solid interconversion from β'- (220 K < T) to α-[H_3(Cat-EDO-TTF)$_2$]BF_4 (T < 220 K) is originated from the interplay of geometric Jahn-Teller-like distortion (from 180˚ to 147˚) of the intra-hydrogen-bond-unit [H_3(Cat-EDO-TTF)$_2$] and magnetic stabilization of Cat-EDO-TTF dimers, where the paramagnetic-to-non-magnetic and low-to-high resistivity transition occurs. The solid line in the temperature dependence of $\chi_M T$ is reproduced by the singlet–triplet (S–T) dimer model with a very strong antiferromagnetic exchange coupling of $2J/k_B$ = -1700 K.

a in Fig. 1) is much larger than that between the π-dimers (4.3 meV, denoted by *b*), suggesting that a very strong dimerization occurs. This type of conductive molecular material composed of a mono-oxidized TTF^+ derivative is very rare due to the strong intermolecular Coulomb repulsion. In the present system, however, the head-to-tail arrangement of the significantly charge-polarized or zwitterionic-like Cat-EDO-TTF skeletons within and between the π-dimer(s) seems to effectively decrease the intermolecular Coulomb repulsions, to allow the construction of the infinite π–π stacking. Also, between the columns, there are some effective intermolecular interactions (*c*–*e* in Fig. 1).

The phase transition occurs around 220 K. Interestingly, upon the transition, the H-bonded unit becomes bent from 180° to 147° at one of the H-bonded oxygen atoms in the H-bond (Fig. 1), which results in desymmetrization of the H-bonded unit: two crystallographically equivalent Cat-EDO-TTF^+ skeletons in the HTP (A and A' molecules) become non-equivalent (A and B molecules), and, simultaneously, the symmetric $[O..H..O]^-$ H-bond is also desymmetrized to an $[O–H..O]^-$ fashion with the O–H and O..H distances of 1.17(4) Å and 1.31(4) Å, respectively. The HOMO energy levels of TTF skeletons are stabilized from -9.310 eV (HTP) to -9.322 and -9.335 eV (LTP: low temperature phase, T < 220 K) by extended Hückel calculation based upon crystal structure analyses. The bent of H-bond unit and stabilization of total energy from the HTP to the LTP are noted to be the Jahn-Teller-like distortion of H-bond unit. Curiously, however, the valence on the TTF skeletons in the LTP is fundamentally unchanged from that in the HTP, to maintain the +1 state, as revealed by the bond length analysis and DFT calculation. Also, the BF_4 anions are still positionally disordered, however, notably the molecular arrangement of the Cat-EDO-TTF^+ skeletons in the conducting layer is dramatically changed: the β'-type arrangement in the HTP, composed of a single kind of π-stack inclined in the same direction, transforms to a so-called α-type molecular arrangement in the LTP, where two types of the π-stacking columns with opposite inclinations (columns A and B) are alternately arranged. In this α-$[H_3(\text{Cat-EDO-TTF})_2]BF_4$ crystal, the tilt angle between the adjacent Cat-EDO-TTF^+ skeletons in the columns A and B corresponds to the bend angle of the H-bonded unit, which thus suggests that this unusual molecular arrangement change is based on the transformation of the H-bonded unit between the planar and bent forms.

Temperature dependence of the electrical resistivity and magnetic susceptibility (Fig. 1) of this H-bonded-unit-based conductor $[H_3(\text{Cat-EDO-TTF})_2]BF_4$ was measured on the single crystal and polycrystalline sample, respectively. In both the measurements, we observed the phase interconversion between the high-temperature β'-$[H_3(\text{Cat-EDO-TTF})_2]BF_4$ and the low-temperature α-$[H_3(\text{Cat-EDO-TTF})_2]BF_4$, in the almost same temperature region. In the resistivity measurement, the resistivity at room temperature is 50 ohm cm and a semiconductor–semiconductor transition with an abrupt change in ρ was observed at around 210 K, which leads to an increase in the activation energy from 135 meV in the HTP to 165 meV in the LTP. This lowering of the transport property is due to the enhancement of the π-dimerization and the decrease of the inter-columnar interaction, which make the conductive π-electrons further localized within the π-dimer. The magnetic properties are also significantly altered around the anomaly at 220–230 K (Fig. 1): after its gradual decrease from 300 K, the $\chi_M T$ value rapidly dropped at 230 K and recorded 0.0 emu mol^{-1} K below 220 K, indicating that the LTP is a non-magnetic state. Also this temperature dependence was reversibly observed. We note here that the $\chi_M T$ value at 300 K (0.047 emu mol^{-1} K) is much smaller than the expected value for non-interacting two S = 1/2 spins (0.75 emu mol^{-1} K), suggesting the occurrence of a strong antiferromagnetic interaction between the S = 1/2 radical cationic TTF^+ skeletons in the π-dimer. Actually, the temperature dependence of $\chi_M T$ in the HTP (T > 220 K) was well reproduced by the singlet–triplet (S–T) dimer model with a very strong antiferromagnetic exchange coupling of $2J/k_B$ = -1700 K (solid line in Fig. 1).

In summary, we have discovered the novel proton-π-electron coupled (PEC) conductor, β'-$[H_3(\text{Cat-EDO-TTF})_2]BF_4$, with the solid-solid interconversion from β'- to α-phase accompanying resistivity and magnetic switching of the BF_4 complex. This transition is derived from geometric Jahn-Teller-like distortion from planar to bent form of the composed hydrogen-bonded unit and the magnetic stabilization towards bond-order derived from spin singlet state with stronger dimerization of molecules. Further systematic tuning of proton and π-electron dynamics in this coupled system will afford novel chemical and physical functionalities beyond the framework of π-electronics so far.

References

[1] H. Kamo, A. Ueda, T. Isono, K. Takahashi, and H. Mori, Tetrahedron Lett. **53**, 4385 (2012).

[2] T. Isono, H. Kamo, A. Ueda, K. Takahashi, A. Nakao, R. Kumai, H. Nakao, K. Kobayashi, Y. Murakami, and H. Mori, Nature Commun. **4**, 1344 (2013).

[3] T. Isono, H. Kamo, A. Ueda, K. Takahashi, M. Kimata, H. Tajima, S. Tsuchiya, T. Terashima, S. Uji, and H. Mori, Phys. Rev. Lett. **112**, 177201 (2014).

[4] A. Ueda, S. Yamada, T. Isono, H. Kamo, A. Nakao, R. Kumai, H. Nakao, Y. Murakami, K. Yamamoto, Y. Nishio, and H. Mori, J. Am. Chem. Soc. **136 (34)**, 12184 (2014).

[5] A. Ueda, A. Hatakeyama, M. Enomoto, R. Kumai, Y. Murakami, and H. Mori, Chem. Eur. J. **21**, 15020 (2015).

[6] J. Yoshida, A. Ueda, A. Nakao, R. Kumai, H. Nakao, Y. Murakami, and H. Mori, Chem. Commun. **55**, 15557 (2014).

Authors
J. Yoshida, A. Ueda, A. Nakao[a], R. Kumai[b], H. Nakao[b], Y. Murakami[b], and H. Mori
[a]Comprehensive Research Organization for Science and Society
[b]Institute of Materials Structure Science, High Energy Accelerator Research Organization

Large Anomalous Hall Effect in the Non-Collinear Antiferromagnet Mn_3Sn at Room Temperature

Nakatsuji Group

In ferromagnetic (FM) conductors, an electric current may induce a transverse voltage drop in zero applied magnetic field: this anomalous Hall effect is observed to be proportional to magnetization M, and thus is not usually seen in antiferromagnets in zero field. Recent developments in theory and experiment have provided a framework for understanding the anomalous Hall effect using Berry-phase concepts [1], and this perspective has led to predictions that, under certain conditions, a large anomalous Hall effect may appear in spin liquids and antiferromagnets without net spin magnetization [2]. Although such a spontaneous Hall effect has now been observed in a spin liquid state [3], a zero-field anomalous Hall effect has hitherto not been reported for

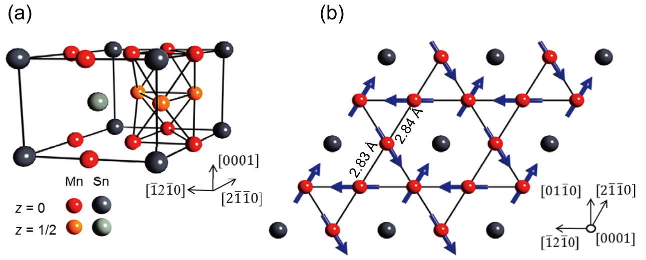

Fig. 1. (a) The crystallographic unit cell of Mn_3Sn. (b) An individual *ab*-plane of Mn_3Sn. Mn moments form an inverse triangular spin structure. Each Mn moment has the local easy-axis parallel to the in-plane direction towards its nearest-neighbor Sn sites.

antiferromagnets.

Mn_3Sn is a hexagonal antiferromagnet (AFM) that exhibits non-collinear ordering of Mn magnetic moments at the Néel temperature of T_N ~ 420 K [4]. The system has a Ni_3Sn-type structure with space group $P6_3/mmc$ (Fig. 1(a)). The basal plane projection of the each *ab*-plane consists of a slightly distorted kagome lattice of Mn, and the associated geometrical frustration manifests itself as an inverse triangular spin structure that carries a very small net FM moment of ~ 2 $m\mu_B$/Mn (Fig. 1(b)) [4]. All Mn moments lie in the *ab*-plane and form a chiral spin texture with an opposite vector chirality to the usual 120° structure. This spin configuration has an orthorhombic symmetry, and only one of the three moments in each Mn triangle is parallel to the local easy-axis. Thus, the canting of the other two spins towards the local easy-axis is considered to be the origin of the weak FM moment [4].

We have carried out detailed transport measurements using high-quality single crystals of Mn_3Sn to reveal the properties associated with the non-collinear antiferromagnetic (AF) ordering [5]. Figure 2(a) presents the field B dependence of the Hall resistivity, $\rho_H(B)$ at 300 K for $B \parallel$ [2-1-10]. $\rho_H(B)$ exhibits a clear hysteresis loop with a sizable jump of $|\Delta\rho_H|$ ~ 6 μΩcm. This is strikingly large for an AFM, and is larger than those found in elemental transition metal ferromagnets (FMs) such as Fe, Co and Ni [1, 6]. Notably, the sign change occurs at a small field of ~ 300 Oe. In contrast, the longitudinal resistivity $\rho(B)$ remains constant except for spikes at the critical fields where the Hall resistivity jumps (Fig. 2(a)). Correspondingly, the Hall conductivity, $\sigma_H = -\rho_H/\rho^2$, for in-plane fields along both [2-1-10] and [01-10] shows a large jump and narrow hysteresis. For instance, with $B \parallel$ [01-10], σ_H has large values near zero field, ~ 20 $\Omega^{-1}cm^{-1}$ at 300 K and nearly 100 $\Omega^{-1}cm^{-1}$ at 100 K. This is again quite large for an AFM and comparable to those values found in FM metals [1, 7]. On the other hand, the Hall signal for $B \parallel$ [0001] shows no hysteresis but only a linear field dependence.

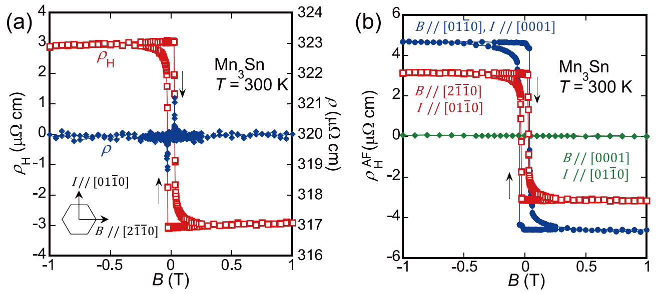

Fig. 2. (a) Field dependence of the Hall resistivity ρ_H and the longitudinal resistivity ρ at 300 K in the magnetic field $B \parallel$ [2-1-10] with the electric current $I \parallel$ [01-10]. (b) Field dependence of the non-collinear AF ordering driven Hall resistivity $\rho_H^{AF} = \rho_H - R_0B - R_s\mu_0M$ at 300 K.

If we label the additional term originating from the non-collinear AF ordering as ρ_H^{AF}, the Hall resistivity in Mn_3Sn can be described by $\rho_H = R_0B + R_s\mu_0M + \rho_H^{AF}$. By subtracting R_0B and $R_s\mu_0M$ from ρ_H, we find that ρ_H^{AF} is nearly independent of B or M, unlike what is found in FMs, as shown in Fig. 2(b). With the reversal of a small applied in-plane field, ρ_H^{AF} changes sign, corresponding to the rotation of the staggered moments of the non-collinear spin structure [4]. Thus, the large AHE, ρ_H^{AF}, must have a distinct AF-driven origin. This soft response of the large anomalous Hall effect in an AFM could be useful for various applications including spintronics—for example, to develop a memory device that produces almost no perturbing stray fields.

Finally, we note that the present exceptionally large AHE found in an AFM with vanishingly small magnetization indicates that a large fictitious field due to Berry phase must exist in momentum space, and is expected to generate various effects including orbital ferromagnetism and the spin Hall effect. Exploration of such effects and their external-field control are suitable subjects for future studies.

References

[1] N. Nagaosa *et al*., Rev. Mod. Phys. **82**, 1539 (2010).
[2] R. Shindou and N. Nagaosa, Phys. Rev. Lett. **87**, 116801 (2001); H. Chen *et al*., Phys. Rev. Lett. **112**, 017205 (2014); J. Kübler and C. Felser, Europhys. Lett. **108**, 67001 (2014).
[3] Y. Machida, S. Nakatsuji, S. Onoda, T. Tayama, and T. Sakakibara, Nature **463**, 210 (2010).
[4] S. Tomiyoshi *et al*., J. Phys. Soc. Jpn. **51**, 2478 (1982); P. J. Brown *et al*., J. Phys. Condens. Matter **2**, 9409 (1990).
[5] S. Nakatsuji, N. Kiyohara, and T. Higo, Nature **527**, 212 (2015).
[6] C. L. Chien and C. R. Westgate, *The Hall Effect and its Applications* (Plenum, 1980).
[7] T. Miyasato *et al*., Phys. Rev. Lett. **99**, 086602 (2007).

Authors

S. Nakatsuji, N. Kiyohara, and T. Higo

Strange Metal Phase without Magnetic Criticality

Nakatsuji and Uwatoko Groups

In condensed matter physics, it is highly important subject to find a novel state of matter. Through many extensive work performed on strongly correlated electron systems including heavy electron metals, high-Tc superconductors and organic conductors, it has been one of the most intriguing and significant possibility that there should be another class of a metallic phase that cannot be described by the standard frame work of metal, namely, Fermi liquid theory. It has been often called as strange metal phase. However, its strong sensitivity to impurity has made it hard to distinguish it from quantum criticality associated with a singular zero temperature point, namely, quantum critical point.

Nakatsuji and Uwatoko groups at ISSP University of Tokyo and a theoretical group at Rutgers University, USA, have studied the pressure effect on heavy fermion system β-$YbAlB_4$ and found the first evidence of a strange metal phase over an extensive region of pressure by suppressing superconductivity. Just as the melting of ice involves a transition from solid to liquid state, strongly correlated materials exhibit transition between magnetic ordered state and a Fermi liquid state. Among the strongly correlated electron systems, the heavy fermion metals often offer the

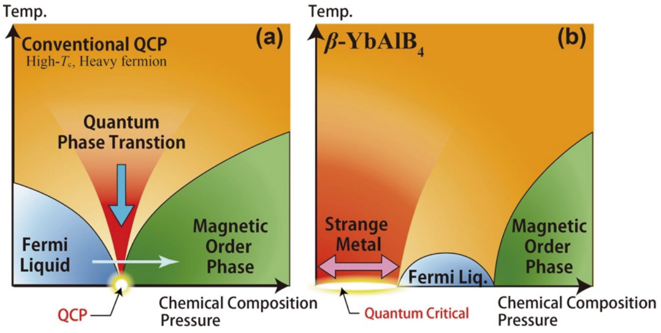

Fig. 1. Conventional quantum critical point and new types of strange metal phase realized in β-YbAlB$_4$

convenient cases where the transition temperature can be easily tuned, for example, by varying a physical parameter, such as magnetic *field*, external *pressure* and chemical composition. In particular, the parameter where the transition temperature is suppressed to absolute zero temperature (minus 273.15 °C) is called quantum critical point (QCP). Nearby the quantum critical point, at low temperatures, a strange metal state is believed to emerge due to quantum critical fluctuations associated with the instability between the magnetic ordered state and Fermi liquid state (Fig. 1(a)). As the quantum critical point is very unstable, the quantum critical phenomena such as the non-Fermi liquid state and superconductivity appear only nearby quantum critical point (conventional QCP in Fig. 1).

Here, we show our experimental study on an ultrapure single crystal of the Yb-based heavy fermion compound β-YbAlB$_4$. β-YbAlB$_4$ is known to have a zero magnetic field and zero pressure quantum critical point and exhibits pronounced strange metal state and superconductivity at low temperatures [1-3]. We applied high pressures and performed high resolution measurements of electric resistivity at low temperatures to investigate its electrical properties. A small magnetic field was used to suppress the superconductivity to reveal the strange metal state. Eventually, we succeeded in elucidating a number of surprising phenomena (Fig. 1(b)) [4]:

1) In the extensive pressure regime ($0 < P < 0.4$ GPa), a strange-metal region with non-Fermi liquid properties exists beneath the superconducting dome.
2) Both the strange metal phase as well as the superconducting (SC) phase ($0 < P < 1$ GPa) are isolated from the border of magnetism ($P > 2.5$ GPa).
3) The strange metal phase can not be described by the standard theory of metals based on spin fluctuations. A new type of mechanism is expected, and is most likely associated with valence fluctuations.

These discoveries imply the existence of a strange metallic phase (Fig. 1(b)), which should be well distinguished from the quantum critical states associated with a magnetic quantum critical point (conventional QCP in Fig. 1(a)). This insight may be useful for clarifying the mechanism for the strange metal phase. It may also contribute to understanding the superconducting mechanisms associated with other classes of strongly correlated materials such as Cu-based and Fe-based high-temperature superconductors.

References

[1] S. Nakatsuji, K. Kuga, Y. Machida, T. Tayama, T. Sakakibara, Y. Karaki, H. Ishimoto, S. Yonezawa, Y. Maeno, E. Pearson, G. G. Lonzarich, L. Balicas, H. Lee, and Z. Fisk, Nature Physics **4**, 603 (2008).
[2] K. Kuga, Y. Karaki, Y. Matsumoto, Y. Machida, and S. Nakatsuji, Phys. Rev. Lett. **101**, 137004 (2008).
[3] Y. Matsumoto, S. Nakatsuji, K. Kuga, Y. Karaki, N. Horie, Y. Shimura, T. Sakakibara, A. H. Nevidomskyy, and P. Coleman, Science **331**, 316 (2011).
[4] T. Tomita, K. Kuga, Y. Uwatoko, P. Coleman, and S. Nakatsuji, Science **349**, 506 (2015)

Authors

T. Tomita, K. Kuga, Y. Uwatoko, P. Coleman[a,b], and S. Nakatsuji,
[a]Rutgers University
[b]University of London

Field Induced Quantum Metal-Insulator Transition in the Pyrochlore Iridate $Nd_2Ir_2O_7$

Nakatsuji and Kindo Groups

Recently, the iridium oxides (iridates) have attracted tremendous attention for their unique position amongst correlated electron materials, balancing comparable electronic kinetic energy (bandwidth), Coulomb interaction (U), and spin-orbit coupling. This makes them susceptible to novel quantum effects, forming topological phases, and phase transitions. $Nd_2Ir_2O_7$ as a member of pyrochlore iridates, is a rare example of a *weak* Mott insulator, which undergoes a continuous metal-insulator transition (MIT) at $T_{MI} \sim 32$ K, the transition closest to the $T = 0$ quantum MIT in this class of materials. Hence, novel quantum critical Mott transitions, quantum spin liquid phases, and other exotic states are expected to emerge in this weak Mott insulator. Here, we report for the first time a quantum phase transition between a magnetic insulating state and a metallic state driven by magnetic field. Our discovery may be potentially important for applications, showing how to tune the metal-insulator transition by applying magnetic field in a weak Mott insulator.

Anisotropic magnetotransport measurements were performed under high magnetic field up to 50 T using high quality $Nd_2Ir_2O_7$ single crystals. Strikingly, a strongly anisotropic field induced quantum metal-insulating transition was discovered in this *cubic* symmetric material. The insulator state can be suppressed by such a field ~ 10 T to a zero temperature quantum MIT only for fields near the [001] axis, as shown in Fig. 1(a). The strong sensitivity to the field direction is remarkable for a cubic crystal, as is the fact that the MIT can be driven by such a small magnetic field, given the 45 meV gap energy, which is ~ 50 times larger than the Zeeman energy for an Ir^{4+} spin.

We mapped out the temperature-field phase diagram for $Nd_2Ir_2O_7$ under magnetic field along the [001] direction. As shown in Fig. 1(b), a systematic change in the MIT from

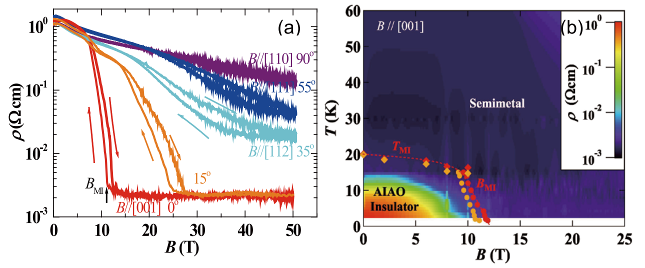

Fig. 1. (a) Field-dependent magnetoresistivity with increasing and decreasing field at T=2 K for various field directions between [001] and [110] directions. The angle Θ is measured from the [001] directions. (b) Temperature-field phase diagram for $Nd_2Ir_2O_7$ under a magnetic field along [001] direction.

continuous near zero field to first order under fields indicates the emergence of possible tricritical point proximate to the quantum phase transition, consistent with the hysteresis seen in the field dependent data shown in Fig. 1(a). Notably, this systematic change across the tricritical point may exist only for the case using high quality single crystals. This new insight contributed to the understanding of quantum MIT behavior. The theorists have constructed a Kondo lattice model considering the strong Kondo coupling between Nd-moments and Ir conduction electron sites, emphasizing the essential role of Nd physics in this quantum MIT picture under magnetic fields.

References

[1] Z. Tian, Y. Kohama, T. Tomita, H. Ishizuka, T. H. Hsieh, J. J. Ishikawa, K. Kindo, L. Balents, and S. Nakatsuji, Nat. Phys. **12**, 134 (2016).

Authors
Z. Tian, Y. Kohama, T. Tomita, H. Ishizuka[a], T. H. Hsieh[a,b], J. J. Ishikawa, K. Kindo, Leon Balents[a], and S. Nakatsuji
[a]Kavli Institute for Theoretical Physics, University of California
[b]Massachusetts Institute of Technology

Emergence of a Kondo Singlet State with $T_K \approx 2000K$ in the Proton-Embedded Electron Gas: Route to High-T_c Superconductivity

Takada Group

Physics in heavy fermion superconductors has been understood by the concept of quantum criticality in a Kondo lattice and the spin-fluctuation mechanism is believed to be responsible for superconductivity, as inferred from the strong correlation between T_c and T_K. More specifically, T_c is of the order of $0.1T_K$, as shown in Fig. 1, from which we can conceive an idea that high-T_c superconductivity will be obtained if we can discover a Kondo system with very high T_K. In fact, the recently-discovered plutonium compounds such as $PuCoGa_5$ with T_c=18.5K and T_K≈260K may be regarded as a successful realization of this idea. Thus we should make further pursuit of this idea by searching for a new class of Kondo systems with T_K higher than 1000K. Theoretically, this search can be done by the first-principles quantitative determination of T_K for the composite system of an impurity atom embedded in a metal.

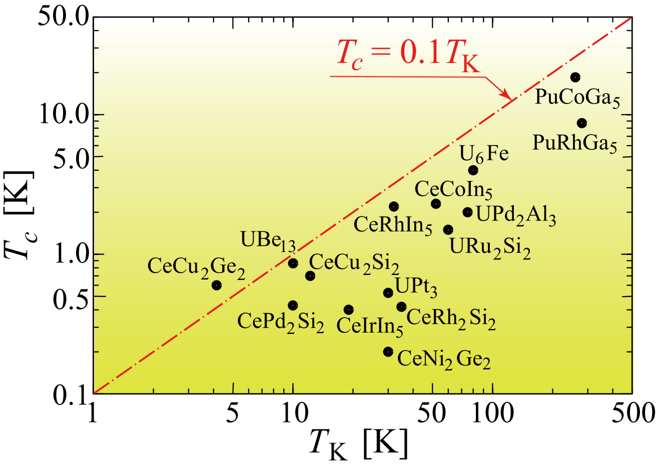

Fig. 1. Superconducting transition temperature T_c versus Kondo temperature T_K (a characteristic energy scale for spin fluctuations) in heavy fermion superconductors.

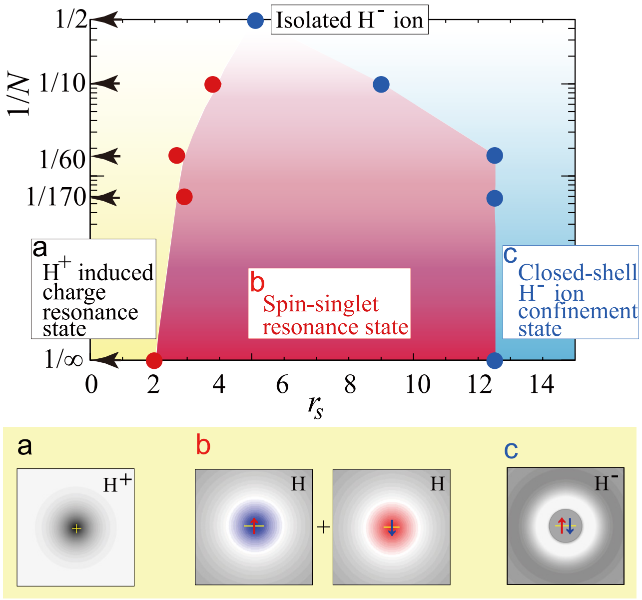

Fig. 2. Phase diagram for sharp sequential transitions among (a) charge resonance, (b) spin-singlet resonance, and (c) closed-shell H^- ion confinement states in the proton-embedded electron gas with N the total number of electrons and r_s the electron density parameter to specify the electron gas.

As first suggested by Debye and Hückel, an atomic nucleus charge $+Ze$ in a metal is screened by accumulation of metallic electrons which is regarded as a charge resonance and well described by the linear response theory. This concept of metallic screening is prevailing for a century, but because Z is not infinitesimally small, we need to consider nonlinear effects in the screening, including the contribution from spin fluctuations. The spin contribution will be enhanced, if Z is an odd integer, such as Z=1 (case of a proton), in which a spin-polarized bound state might appear at the impurity atom.

With the above basic scientific issues in mind, we have concerned with the problem of hydrogen impurity in metals which attracts long attention from a technological point of view, such as hydrogen storage in solids, sensor applications, and catalysis. Its electronic state has been investigated in terms of a proton immersed into the electron gas since 1970s, but no serious attention has been paid so far to the spin resonance effect.

We have studied this system with changing the electron density in a wide range by employing the diffusion Monte Carlo simulations with the total electron number N up to 170 to accurately obtain the ground-state electronic distribution $n(\boldsymbol{r})$ and found a sharp transition at r_s≈2 from short-range H^+ screening charge resonance to long-range Kondo singlet resonance, the emergence of which is confirmed by the presence of an oscillation-period-shortened Friedel oscillation characteristic to the Kondo singlet state with T_K well beyond 1000K for r_s in the range 3-8. Another transition to the closed-shell H^- confinement state occurs at r_s≈12.5 (see Fig. 2).

This study not only reveals interesting competition between charge and spin resonances, enriching the century-old paradigm of metallic screening to a point charge, but also discovers a long-sought high-T_K system, opening a new and unexpected route to room-temperature superconductivity in a Kondo lattice made of protons. The metal hydrides, usually used for secondary batteries, are promising candidates, if the metallic electron density is suitably arranged and the lattice constant is properly tuned to exhibit quantum criticality in the Kondo lattice.

References

[1] Y. Takada, R. Maezono, and K. Yoshizawa, Phys. Rev. B **92**, 155140 (2015).

Authors
Y. Takada, R. Maezono[a], and K. Yoshizawa
[a]Japan Advanced Institute of Science and Technology

Chiral Magnetic Effect in Condensed Matter Systems

Oshikawa Group

Relativistic massless fermions in 3+1 dimensions exhibit so-called chiral anomaly where the chiral symmetry, which is a symmetry of the Lagrangian, is broken due to quantum effects. This results in the violation of the individual conservation of the number of left-handed and right-handed fermions, allowing them to change to each other. Chiral magnetic effect (CME), an induction electric current parallel to the applied external magnetic field is one of the most intriguing phenomena related to this chiral anomaly. Due to the time reversal symmetric nature of CME, the current induced through CME is non-dissipative so that it has potential applications to the low-energy consuming electronics.

Recently, it becomes possible to synthesize a family of three-dimensional materials, topological semimetals, where electrons have (3+1) dimensional relativistic band dispersion near the Fermi energy, similar to graphene in (2+1) dimensions. That is, in these materials, the relativistic massless fermions emerge in the low-energy effective theory. It is thus tempting to observe the chiral anomaly and CME in a tabletop experiment with a high-controllability which we cannot have in high-energy physics. Indeed, there are already several experimental reports that claim to have observed the chiral anomaly and CME in topological semimetals through the negative magnetoresistance in the presence of parallel electric and magnetic field. Although the negative magnetoresistance can be an indication of the chiral anomaly, it could arise from other mechanisms and thus is not a smoking-gun evidence for the chiral anomaly, let alone CME

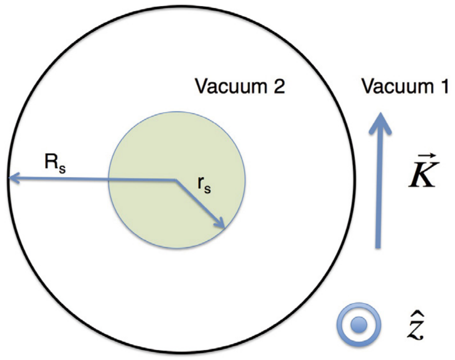

Fig. 1. Schematic picture of our setup. A solenoid (radius R_s) is represented as a surface current K between the two vacua. Inside them, a cylindrical sample (radius r_s) is placed.

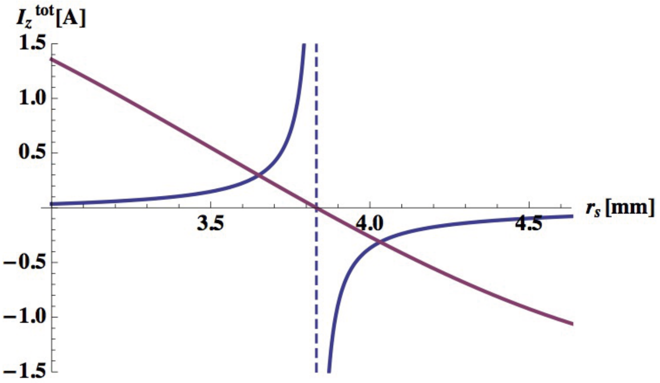

Fig. 2. Blue line: Total current Itotz [A] for parameters $\mu_0\sigma_{ch} = 1$ [mm], ω=100 [Hz], B = 1 [Gauss]. Red: $J_1(\mu_0\sigma_{ch}r_s)$ in an arbitrary unit. The current is resonantly enhanced for rs satisfying $J_1(\mu_0\sigma_{ch}r_s) = 0$ represented by a dashed line.

In order to develop a direct and unambiguous probe of CME, we studied the interplay of CME and electromagnetism in matter. Since CME can be understood as a consequence of an extension of electromagnetism called Chern-Simons electromagnetism, transport properties are governed in a highly non-trivial manner by both electromagnetism and CME. As a concrete example, we performed an electromagnetic field analysis in the setup shown in Fig. 1. We demonstrated that the physically observed admittance is not simply proportional to the chiral magnetic conductivity, even when the transport is governed by the CME. Furthermore, we found that the CME-induced AC current is resonantly enhanced when the cross section matches the "chiral magnetic length" as shown in Fig. 2. Our results imply that the electromagnetism is fundamental for actual transports in topological semimetals and that proposals for their applications to future electronics need careful considerations on this issue.

Reference

[1] H. Fujita and M. Oshikawa, arxiv: 1602.00687

Authors
H. Fujita and M. Oshikawa

Optical Conductivity Near an Antiferromagnetic Phase Transition

Tsunetsugu Group

Optical conductivity is one of fundamental dynamical correlation functions in solids and measures a metallicity. A few years ago, we numerically investigated optical conductivity near the Mott metal-insulator transition in the frustrated Hubbard model on a triangular lattice using a cluster dynamical-mean field theory (CDMFT). We found a singularity in its dc value and in contrast to general belief the corresponding critical exponent does not coincide with that of the order parameter [1]. Another important finding was that the vertex corrections are not so important in that case. The Mott transition is driven by strong correlation effects, which may suggest large vertex corrections. However, our numerical data exhibited only a minor contribution of theirs, and it is likely due to two characteristic features in this system. The first is that spin fluctuations depend little on wave vectors because of strong frustration. The second is that quasiparticle scatterings due to spin fluctuations do not depend so much on their position on the Fermi surface. We have performed a new study to examine if the vertex corrections are more pronounced in an unfrustrated system. To compare with the previous result, we particularly investigated the temperature region near an antiferromagnetic phase transition.

We have used a 4-site CDMFT approach for calculating optical conductivity σ(ω) in the square-lattice Hubbard model at half filling, and studied its temperature dependence both above and below the antiferromagnetic transition temperature T_N for the Coulomb repulsion U=6.5t. Here, t is the matrix element of nearest-neighbor hopping. A real antiferro long-range order is absent in two-dimensional systems, and our results correspond to quasi-two-dimensional systems. To implement the vertex corrections in the antiferromagnetic phase, we have derived a new formula based on our previous one for the paramagnetic phase. We have found that the vertex corrections change various important details in temperature and frequency dependence of conductivity near T_N. This point differs from our previous study on optical conductivity near the Mott transition in a frustrated triangular lattice.

General trends in the temperature evolution of σ(ω) are consistent with expected behaviors near the metal-insulator transition. In the high-temperature paramagnetic phase, σ(ω) has the Drude peak at ω=0 and also a broad peak around ω~U, which is related to excitations to the Hubbard bands. With lowering temperature, an antiferromagnetic phase transition occurs at T_N~0.34t, and σ(ω) changes its frequency dependence below T_N. While the incoherent peak continues to exist, now a dip appears at ω=0 and the low-energy peak shifts to ω~t. Top two panels in Fig. 1 compare σ(ω) with and without the vertex corrections. Most importantly, the vertex corrections enhance variations in the frequency dependence. The Drude peak and the high-ω broad peaks in the paramagnetic phase are both sharpened. This continues in the antiferromagnetic phase and the two peaks are both sharpened by the vertex corrections, whereas the dip at ω=0 is also enhanced. Another important discovery is the behavior in a temperature region just above T_N. As shown in the bottom panel in Fig. 1, dc conductivity decreases in this region with lowering temperature, which is a precursor of the transition. However, the electron excitation spectrum shows no pseudogap behavior and the Drude peak is pinned at ω=0. This temperature region appears before including the vertex corrections, but the corrections extends it quite wide. These are main results directly related to observable properties in experiments.

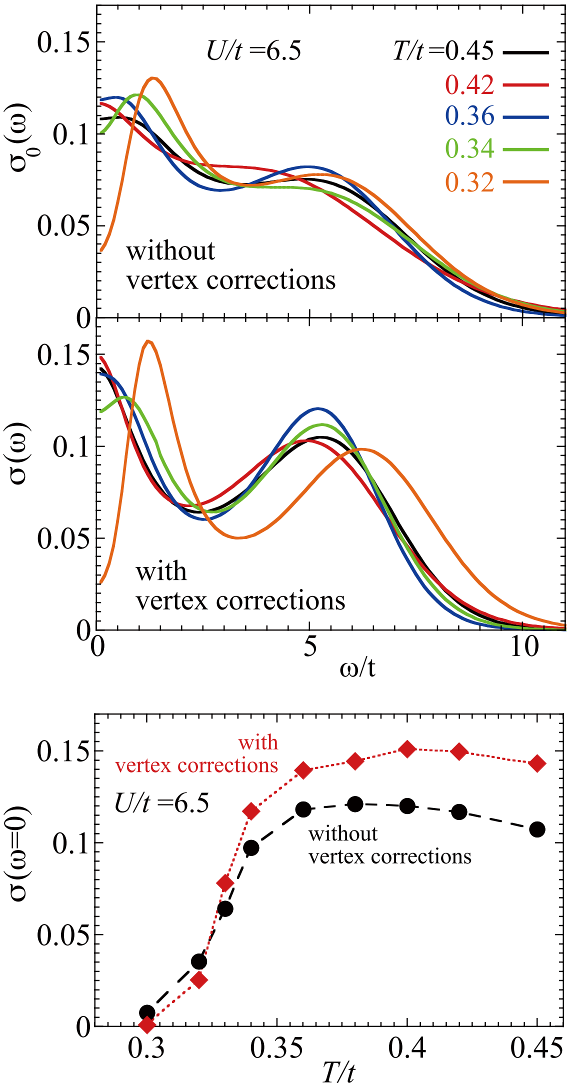

Fig. 1. (Top) Optical conductivity in the square-lattice Hubbard model at half filling. Units are the quantum conductance. (Bottom) Temperature dependence of dc conductivity in the same model.

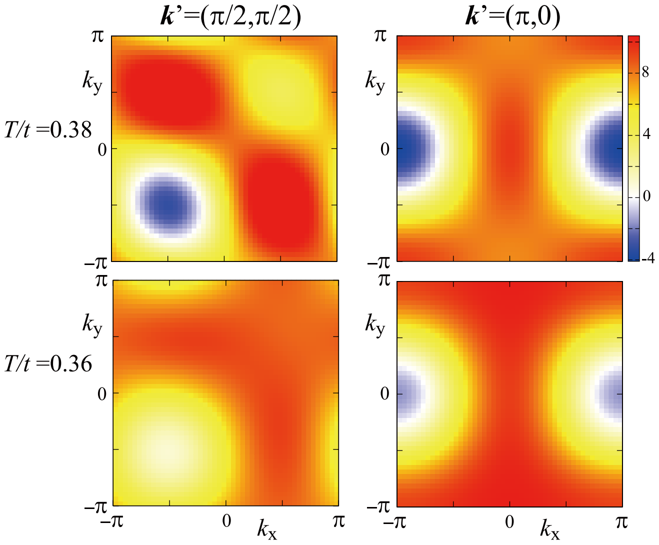

Fig. 2. Momentum dependence of the vertex function Γ that describes the process that a particle-hole pair with momentum and spin (***k***', σ') are scattered to another pair with (***k***, σ). Plotted is the charge part summed over σ and σ' at Matsubara frequency ν_n=0. Dependences on temperature and ***k***–***k***' strongly vary with the initial momentum ***k***'.

For better understanding of the vertex corrections, we have also carried out their detailed analysis. The vertex corrections are determined by the vertex function Γ and four single-electron Green's functions. As for the part of the Green's functions, we have found that their spin dependent components provide a dominant contribution in the antiferromagnetic phase. For Γ a predominant contribution is given by the scattering processes of polarization made of a particle on one sublattice and a hole on the other sublattice. We have also examined Γ's momentum dependence. Results in the paramagnetic phase are shown in Fig. 2. In the antiferromagnetic phase, the charge vertex and spin vertex functions have similar momentum dependence but the sign is opposite. A large difference is found in Γ's momentum dependence between quasiparticles at different positions in the Brillouin zone. For those at (π, 0) or (0, π), the momentum dependence is dominated by nearest-neighbor correlations. For those at (π/2, ±π/2), the momentum dependence is quite one-dimensional. It is an important future study to clarify how to relate these exotic correlations to properties of conductivity.

This work is collaboration with Toshihiro Sato at RIKEN.

Reference

[1] T. Sato, K. Hattori, and H. Tsunetsugu, Phys. Rev. B **86**, 235137 (2012); J. Phys. Soc. Jpn. **81**, 083703 (2012).

Author

H. Tsunetsugu

Temperature-Driven and Chemical-Potential-Driven Adiabatic Pumping in Coherent Electron Transport

Kato Group

Adiabatic pumping is a process by which a finite charge(heat) current is induced under periodic slow modulation of external parameters. This phenomenon has been studied for a long time as an important issue in time-dependent quantum transport. In addition to charge current, recent developments in the field of nanotechnology have enabled us to measure heat current under temperature bias in a controlled way. This development has stimulated both of the theoretical and experimental investigations of the thermodynamics properties of mesoscopic devices. Recently, adiabatic heat pumping induced by temperature modulation has been discussed in phonon transport via molecule junctions [1], and temperature-induced transport has been discussed in contexts of thermoelectric transport and nonequilibrium thermodynamics [2].

We have studied adiabatic charge pumping driven by modulation of thermodynamic variables of the reservoirs in the *coherent* regime [3]. We have considered charge pumping via a single-level quantum dot (QD) coupled to reservoirs with time-dependent temperatures and chemical potentials (see Fig. 1), and have shown that charge pumping is indeed possible when Coulomb interaction is introduced in the QD. We have calculated pumping current up to the first order of U (the strength of the Coulomb interaction in the QD) by the perturbation theory based on the Keldysh formalism, employing the method of the thermomechanical field to describe temporal changes of the temperatures.

We show the estimated average pumping current in Fig. 2 for a pumping frequency f=1GHz. The upper panel of Fig. 2 shows the pumping current under the chemical-potential modulation described by $\mu_L(t)=\mu_0+\mu_1\cos(2\pi ft)$ and $\mu_R(t)=\mu_0+\mu_1\sin(2\pi ft)$ for $\mu_1=0.5\Gamma$ and $T_L=T_R(=T)=0$, 0.1Γ, 0.3Γ as a function of $(\mu_0-\varepsilon_d)/\Gamma$, where ε_d and Γ are an energy level and a linewidth of the QD, respectively. The lower panel of Fig. 2 shows the pumping current under the temperature modulation described by $T_L(t)=T_0+T_1\cos(2\pi ft)$ and $T_R(t)=T_0+T_1\sin(2\pi ft)$ for $T_1=0.3\Gamma$, $\mu_L=\mu_R=0$, and $\varepsilon_d=0$, 0.1Γ, 0.3Γ as a function of T_0. In the present estimate, we have assumed the symmetric coupling to the two reservoirs, and have set the strength of Coulomb interaction as U=Γ. As seen in Fig. 2, the estimated pumping current is of order of 1-10pA, which is measurable in a standard experimental setup. The pumping current is proportional to both the frequency f and the Coulomb interaction U in the present calculation, and therefore is reduced if f and U are taken as smaller. In the chemical-potential-driven pumping, we have shown that the pumping current is related to the first energy derivative of the spectral function (the local density of states in the QD) at low temperatures. Similarly, in the temperature-driven pumping, we have shown that the pumping current is related to the second energy derivative of the spectral function at low temperatures; the sign change of the pumping current for $\varepsilon_d=\Gamma$ in the lower panel of Fig. 2 originates from this fact. The insets of Fig. 2 show the time-dependence of the current induced by the modulation at the maximum of the pumping current in the main panel.

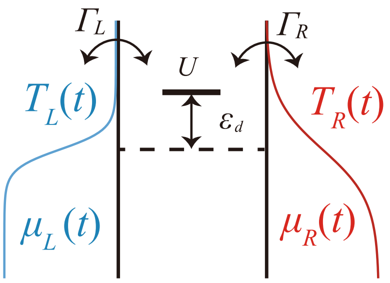

Fig. 1. Schematic figure of the system considered in this study.

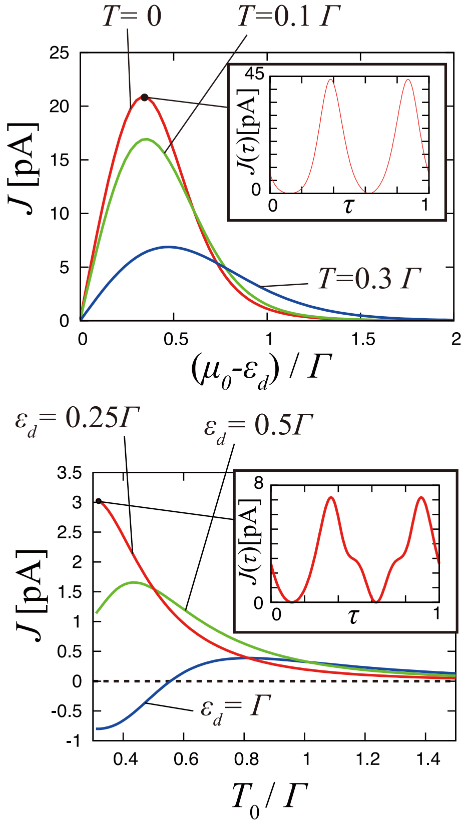

Fig. 2. The upper panel: Estimated pumping current under the chemical-potential modulation described by $\mu_L(t)=\mu_0+\mu_1\cos(2\pi ft)$ and $\mu_R(t)=\mu_0+\mu_1\sin(2\pi ft)$ for $\mu_1=0.5\Gamma$ and $T_L=T_R=0$, 0.1Γ, 0.3Γ as a function of $(\mu_0-\varepsilon_d)/\Gamma$. Here, ε_d and Γ are an energy level and a linewidth of the QD, respectively. The lower panel: Estimated pumping current under the temperature modulation described by $T_L(t)=T_0+T_1\cos(2\pi ft)$ and $T_R(t)=T_0+T_1\sin(2\pi ft)$ for $T_1=0.3\Gamma$, $\mu_L=\mu_R=0$, and $\varepsilon_d=0$, 0.1Γ, 0.3Γ as a function of T_0.

We have also shown that the present charge pumping originates from a time delay in a change of the occupation number of the QD with respect to modulation of the reservoirs. This time delay is understood by a relaxation time determined by circuit elements characteristic of coherent electron transport under external AC modulation of voltages and temperatures.

In this study, we have studied charge pumping in a simple setup with a single-level QD up to the leading order of Coulomb interaction. It is a future problem to formulate adiabatic pumping in the presence of a strong Coulomb interaction. Also, with the present formulation, we would be able to tackle general pumping in coherent transport from the viewpoint of the nonequilibrium thermodynamic properties of mesoscopic devices.

References
[1] J. Ren, P. Hänggi, and B. Li, Phys. Rev. Lett. **104**, 170601 (2010).
[2] T. Yuge, T. Sagawa, A. Sugita, and H. Hayakawa, J. Stat. Phys. **153**, 412 (2013).
[3] M. Hasegawa and T. Kato, arXiv:1601.05812 (2016).

Authors
M. Hasegawa and T. Kato

"Zitterbewegung" Appeared as Conductance Fluctuation in Transport Between Quantum Point Contacts

Katsumoto Group

For a particle which obeys the Dirac equation, velocity is not a well-defined quantity in that the kinetic motion in real space is the mixed one of particle and anti-particle. Such a quantum mechanical state can be described as a superposition of states with velocities +*c* and –*c*. Hence in the space of velocity-base, such a particle is in a zigzag motion (trembling motion), which is called "Zitterbewegung" (ZB) in Germany[1]. A trivial analog in electrons in solids is oscillation in velocity of classical electrons due to periodic lattice potential. Even the experimental observation of such a trivial phenomenon is difficult at present. A bit non-trivial phenomenon closer to the ZB of electrons in vacuum is a zigzag motion of electrons due to the spin-orbit mixing of the two (spin and orbital) freedoms. This is also called ZB and expected to be observable in experiments though no clear observation has been reported yet.

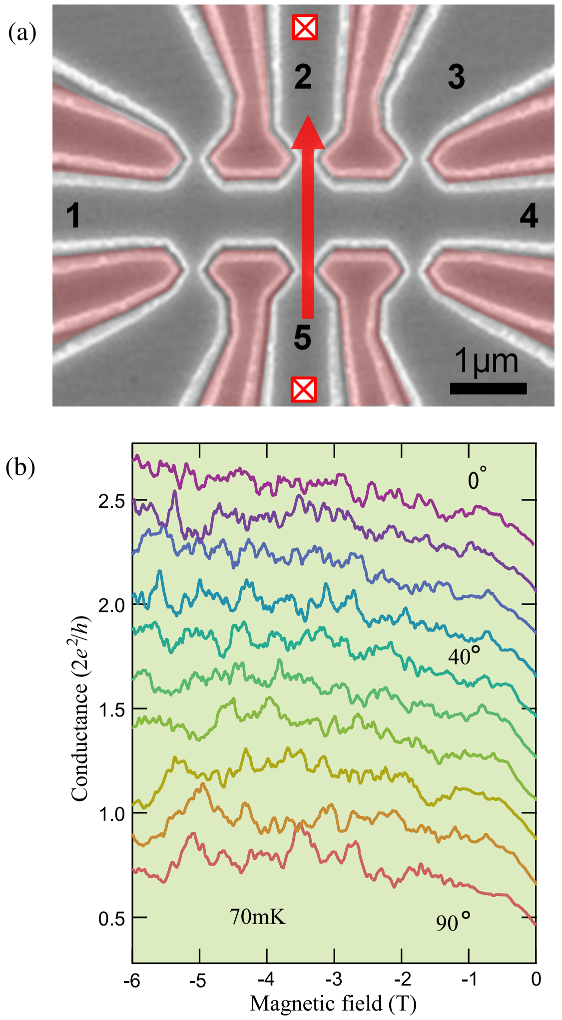

Fig. 1. (a) QPC positioning in the sample. (b) Conductance fluctuation (through QPC 2 to 5) versus magnetic field. The field is rotated from 0° (parallel to the plane) to 90° (perpendicular).

For the observation of ZB in transport, we need to prepare spin-polarized electrons in a system with a simple-form spin-orbit interaction. We have experimentally confirmed that a quantum point contact (QPC) in a system with strong Rashba-type spin-orbit interaction (RSOI) can work as an efficient spin polarizer on plateaus of a half and of a one conductance quantum ($2e^2/h$) [2]. Hence a system of QPCs with RSOI can provide an ideal test-bed of ZB in solids.

Figure 1(a) shows a schematic view of the present system with two sets of three parallel QPCs made from InAs 2DEG. The two are placed face-to-face. The two-terminal conductance through a confronting QPC pair (2-5) as a function of magnetic field for various field directions is shown in Fig.1 (b). Reproducible fluctuations reminiscent of universal conductance fluctuation (UCF) appear in the magneto-conductance. Surprisingly the amplitude nor the characteristic frequency does not change with the field angle. On the other hand in the transport not through QPC (terminal 1 to 4) no fluctuation appears and ordinal Shubnikov-de Haas oscillation appears for vertical magnetic field. In short the fluctuation appears only when the spins of conduction electrons are aligned.

The above results can be well explained within the ZB framework. The external magnetic field modifies the frequency of spin precession thus that of ZB, which results in large variation of scattering cross section. Superposition of various scattering paths leads to the observed conductance fluctuation.

References
[1] W. Zawadzki and T. M. Rusin, J. Phys.: Condensed Matter **23**, 143201 (2011).
[2] M. Eto, T. Uehara, H. Taniguchi, K. Satoh, Y. Ishii, and I. Watanabe, J. Phys. Soc. Jpn. **84**, 053703 (2015).

Authors
Y. Iwasaki, Y. Hashimoto, T. Nakamura, and S. Katsumoto

Distant-Dependent Tunneling Process Observed in Iron Nitride

Komori Group

Scanning tunneling microscopy (STM) is one of the most powerful tools to investigate surface topographic and electronic structures with an atomic resolution. Surface nanostructures are often discussed based on the topographic image. However, its image contrast is mainly based on the electron tunneling processes between the STM tip and the surface local electronic states [1]. Systematic changes of the image contrast as a function of the sample-bias voltage *V*s have been widely interpreted in terms of energy-dependent electronic structures. The STM tip-surface distance, *d*, is

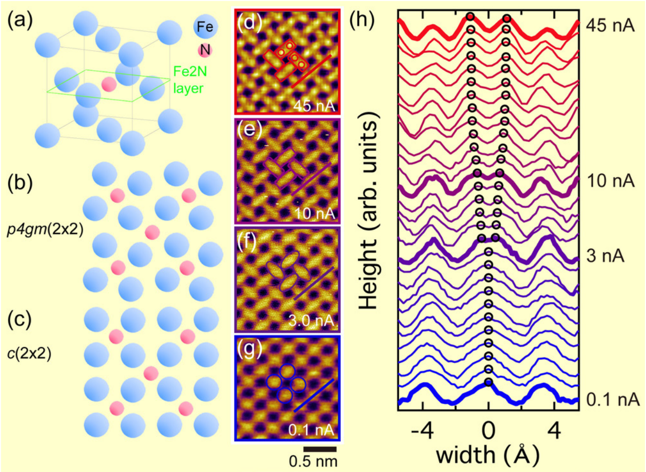

Fig. 1. (a) Schematic model of an Fe_4N crystal. The layer consisting of Fe_2N stoichiometry, indicated by green lines, appears at the surface of the Fe_4N thin films on Cu(001). (b,c) Schematic surface models of the *p4gm*(2x2) reconstruction (b) corresponding to the monatomic Fe_2N layer on Cu(001), and *c*(2x2) reconstruction (c) corresponding to the ideal bulk Fe_2N plane. (d-g) Topographic images taken at *Vs* = 0:25 V with varying *It* from 0.1, 3.0, 10 to 45 nA. (h) Line profiles at *Vs* = 0:25 V, measured along lines indicated in (d-g). From the top to the bottom, *I* varies as follows: 45, 40, 35, 30, 28, 25, 22, 20, 18, 15, 12, 11, 10, 9.0, 8.0, 7.0, 5.0, 3.0, 2.0, 1.0, 0.9, 0.8, 0.7, 0.6, 0.5, 0.4,.0.3, 0.2, and 0.1 nA, respectively. Empty circles indicate peak positions extracted from one Fe dimer.

an alternative parameter of the image change on the surface consisting of several orbitals with different decay lengths of the wave functions into the vacuum. In such systems, the image can be changed by the shift of the dominant surface orbital contributing to the tunneling process. We have demonstrated the *d*-dependent STM imaging and spectroscopy on the surface of a monatomic layer of iron nitride (Fe_2N) on Cu(001) (see Fig. 1) to characterize the orbital-sensitive tunneling as the origin of the topographic image changes [2].

Figure 1(d-g) shows a systematic change of the topographic images of the Fe_2N layer from a dimerized atomic image reflecting the atomic surface structure to a square lattice of atomic size dots with increasing *d*. The line profiles shown in Fig. 1(h) are systematically changing with the tunneling current. By measuring the images with various V_B values, the threshold distance of the image change was found to be independent of V_B . The tunneling spectrum on the Fe_2N surface has several peaks that well correspond to the peaks of the calculated total local density of states (LDOS) as in Fig. 2(a,b). The observed systematic *d* dependence of the tunneling spectra shown in Fig. 2(c) implied the shift in the dominant electronic states contributing to the tunneling process. The LDOS calculations above the surface by first principles indicate the change of the dominant orbitals detected by the STM tip from the Fe 3*d* states to the *s/p* states with increasing the tip-surface distance.

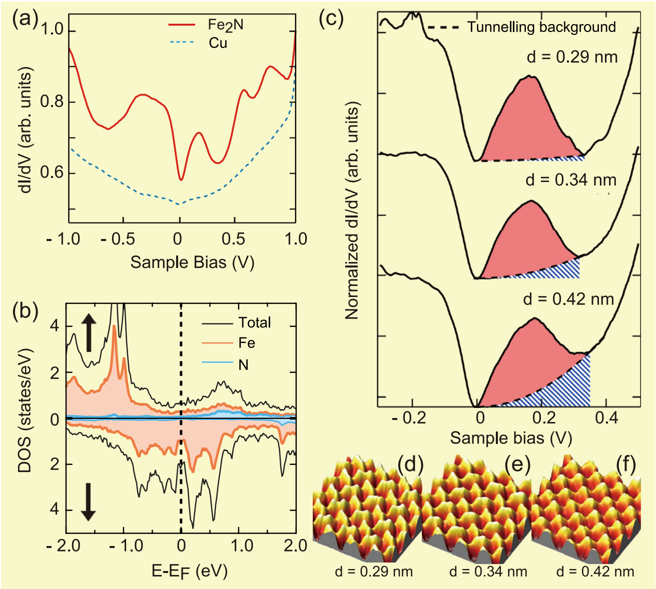

Fig. 2. (a) *dI/dV* spectra of Fe_2N on Cu (001) and the clean Cu(001) surface. The STM tip was stabilized at *It* = 30 nA and *Vs* = 1 V. (b) Calculated spin-resolved LDOS of single-layer Fe_2N on Cu(001). Fe and N states are separately shown. (c) Distant-dependent *dI/dV* spectra measured at d = 0.42, 0.34, and 0.29 nm from the bottom to the top. Dashed curves indicate a tunneling background obtained by a Tersoff-Hamann approximation. [1] (d-f) Topographic images taken at *Vs* = 0.25 V with *d* = 0.29 nm (d), 0.34 nm (e), and 0.42 nm (f).

References

[1] J. Tersoff and D. R. Hamann, Phys. Rev. B **31**, 805 (1985).
[2] Y. Takahashi *et. al.*, Phys. Rev. Lett. **116**, 056802 (2016).

Authors

F. Komori, Y. Takahashi, T. Miyamachi, K. Ienaga, N. Kawamura[a], and A. Ernst[b]
[a]Science & Technology Research Laboratories, NHK,
[b]Max-Planck-Institut fur Mikrostrukturphysik

Real-Time Operando Observation of Reaction Processes of CO_2 on Cu(997) by Near-ambient Pressure X-ray Photoelectron Spectroscopy

Yoshinobu and I. Matsuda Groups

Activation of CO_2 is an important topic in the efficient use of CO_2 as a chemical feedstock. Methanol synthesis from CO_2 and H_2 on a Cu/ZnO catalyst has been widely studied. CO_2 is chemically inert, and thus the interaction of the molecule with metallic Cu surfaces plays an essential role for molecular activation. On metallic copper, very low reactivity of CO_2 on low-index surfaces was reported under ultrahigh vacuum conditions. In contrast to the flat surfaces, the dissociation of CO_2 into CO was reported on vicinal Cu surfaces previously. These results indicate that defect sites, such as step and kink, may be important for the CO_2 activation. However, the reaction condition in UHV is far from a real catalytic reaction, which is normally operated at higher temperature and nearly/above atmospheric pressure. Such differences in pressure and temperature may lead to distinct

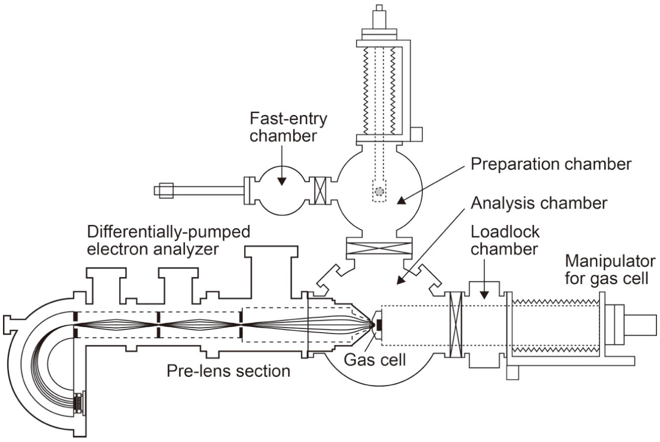

Fig. 1. Schematic of the *operando* AP-XPS system at SPring-8 BL07LSU

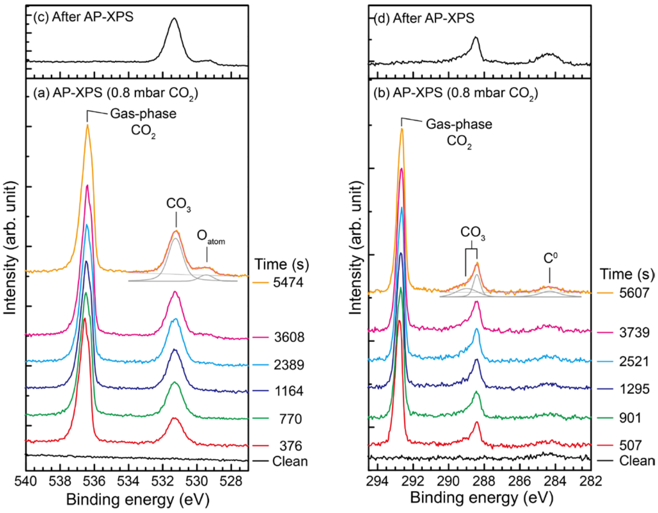

Fig. 2. A series of **(a)** O 1s and **(b)** C 1s AP-XPS spectra of Cu(997) at 340 K under CO_2 pressure of 0.8 mbar as a function of elapsed time together with the assignment of each peak. Only selected spectra from the whole series are shown in the figure. The photon energy was 630 eV. The CO_2 gas was introduced in the gas cell at t = 0 s. The fitting results for the spectra at t = 5474 s (O 1s) and t = 5607 s (C 1s) are also shown in the figure. **(c)** O 1s and **(d)** C 1s XPS spectra after the AP-XPS measurements shown in (a) and (b). The gas cell was evacuated to UHV ($\sim 10^{-9}$ mbar), and then the XPS measurements were performed.

reactivity under ambient conditions from UHV, reflecting thermodynamic and kinetic effects. Ambient pressure X-ray photoelectron spectroscopy (AP-XPS) is a powerful tool for investigating electronic structures and chemical states of adsorbates and a substrate *quantitatively* under reactant-gas pressure.

Here, the reaction of CO_2 on the vicinal Cu(997) surface at 340 K under CO_2 gas pressure of 0.8 mbar was investigated by ambient pressure X-ray photoelectron spectroscopy (AP-XPS). We found that initially carbonate (CO_3) was produced on the surface through the reaction of CO_2 with oxygen formed from CO_2 dissociation; the amount of adsorbed CO_3 was increased and saturated as time elapsed and after saturation of adsorbed CO_3, atomic oxygen appeared on the surface, indicating that CO_2 dissociation into CO and O continued to take place. The estimated saturation coverage of CO_3 from XPS is rather small (0.05 ML).

The experiments were performed using a newly developed AP-XPS apparatus at the soft X-ray undulator beamline BL07LSU of SPring-8. Figure 1 shows a schematic of the present *operando* AP-XPS system at SPring-8 BL07LSU. The AP-XPS system consists of four interconnected UHV chambers; an analysis chamber, a preparation chamber, a load-lock chamber, and a fast-entry chamber. The analysis chamber is used for XPS measurements both in UHV and at ambient conditions. The preparation chamber is equipped with an ion source and low energy electron diffraction optics. The load-lock chamber and the fast-entry chamber allow the introduction of samples from the air into the UHV system.

Figures 2(a) and (b) show series of O 1s and C 1s AP-XPS spectra of the Cu(997) surface at 340 K under CO_2 pressure of 0.8 mbar as a function of elapsed time. Gas-phase CO_2 peaks were initially observed at 536.6 eV in an O 1s XPS spectrum at t = 376 s, and at 292.8 eV in a C 1s XPS spectrum at t = 507 s. These gas-phase peaks were shifted to 536.4 eV and 292.6 eV, respectively, after a lapse of about 5500s. At t = 376 s, a peak of adsorbate was observed at 531.3 eV in the O 1s region. Three peaks of adsorbates were observed in the C 1s spectrum (t = 507 s) at 288.4 eV with a broader shoulder peak at higher binding energy (289.0 eV), and at 284.4 eV (C^0), which is assigned to neutral carbon species such as carbon atoms and hydrocarbons. As discussed later, the other adsorbate peaks at 531.3, 289.0 and 288.4 eV are assigned to carbonate (CO_3). The amount of CO_3 was saturated at t ~ 2000 s, and then a new peak at 529.5 eV appeared in O 1s spectra. This peak is attributed to atomic oxygen. Figures 2(c) and (d) show O 1s and C 1s spectra measured under UHV ($\sim 10^{-9}$ mbar) after a series of AP-XPS measurements. The adsorbates formed in the presence of 0.8 mbar CO_2 were stable at 340 K and remained on the surface even after evacuating the gas cell to UHV. The result indicates that the decomposition of CO_3 does not occur at 340 K.

The composition ratio between oxygen and carbon at the saturation region (t > 2000 s) was calculated from the area intensity of the O 1s peak at 531.3 eV and the sum of the intensities of the two C 1s peaks at 289.0 and 288.4 eV. In the estimation, the O 1s and C 1s intensities of the adsorbate peaks were normalized by those of the gas-phase CO_2 peaks in these spectra to cancel out differences in the analyzer transmission function and the core-election ionized cross section between O 1s and C 1s. The O/C ratio was estimated to be 3.1 ± 0.1. Similar experiments were done using a photon energy (hν) of 740 eV to check the effect of photoelectron diffraction on the estimation of the O/C ratio. The estimated ratio at hν = 740 eV is 3.2 which is within the error in the case of hν = 630 eV. If the observed two peaks in C 1s are due to both CO_3 and chemisorbed CO_2, the O/C ratio should be in the range from 2 to 3. Thus, the peaks at 531.3, 289.0 and 288.4 eV are assigned to CO_3.

The produced CO_3 is stable at 340 K even after evacuation to UHV as shown in Figs. 2(c) and (d). The gas-phase peaks in AP-XPS spectra (Figs. 2a and b) are shifted to lower binding energies with increasing the CO_3 coverage, indicating the increase of the work function by the CO_3 adsorption. Therefore, adsorbed CO_3 is negatively charged by charge transfer from the Cu substrate. The present study clearly shows a facile formation of CO_3 on the stepped Cu surface, and CO_3 may be a key intermediate in CO_2 activation.

Reference

[1] T. Koitaya *et al.*, Top. Catal. **59**, 526 (2016).

Authors

T. Koitaya, S. Yamamoto, Y. Shiozawa, K. Takeuchi, R.-Y. Liu, K. Mukai, S. Yoshimoto, K. Akikubo, I. Matsuda, and J. Yoshinobu

---

Chiral Spin Spiral Structure Studied by Spin-Polarized Scanning Tunneling Microscopy

Hasegawa Group

Because of the potential application for future spintronics devices, spiral magnetic structures, such as skyrmion lattices, domain walls, and homogeneous spin spiral structures, have been a subject of extensive studies. Various types of spin rotations have been reported; Bloch-type (helical) or Néel-type (cycloidal), left-handed (↑←↓) or right-handed (↑→↓), and chiral or non-chiral. To determine these types, neutron scattering, Lorentz microscopy, *etc.* have been utilized. For nanometer- or atomic-scale spin spiral structures, often formed in ultrathin films, spin-polarized scanning tunneling microscopy (SP-STM), which detects spin orientations in atomic-scale spatial resolution, is the only method for the determination. We have investigated the types of the spin structure observed in a monolayer (ML) Mn thin film formed on a tungsten substrate using the ultimate spin-probe microscopic method.

In magnetic systems whose inversion symmetry is broken, the Dzyaloshinskii–Moriya interaction (DMI) plays a key role in the formation of chiral spin structures. Since the symmetry is naturally broken at interfaces, several systems composed of 3d magnetic thin films and 5d non-magnetic heavy-elemental substrates showing a strong spin-orbit coupling exhibit DMI-driven chiral spin structures. For the investigation of how overlayers and substrates affect the polarity and strength of DMI a W(110) substrate is one of the ideal systems because various chiral structures have been discovered on it with overlayers. From SP-STM images taken with a tip whose magnetization direction is well controlled, we revealed that the Mn monolayer indeed exhibits a cycloidal spin spiral structure with a left-handed rotation (See a schematic shown in Fig. 1(e)). By comparing with *e.g.* the case of magnetic domain walls observed in Fe thin films, we found that the polarity of DMI is basically determined by the substrate.

The SP-STM experiments were performed with an ultrahigh vacuum STM at 5 K using Fe-coated W tips as a magnetic probe. Since the amount of the tunneling current is proportional to the cosine of the angle θ between the tip and sample magnetization directions, one can obtain the spin or magnetic contrast of the sample using the magnetized tip. A two-axis superconducting magnet was used to align the tip magnetization to the specific orientations of the sample.

A typical STM image taken on monolayer Mn-covered W(110) surface is shown in Fig. 1(a). A cross-sectional profile shown in Fig. 1(b) indicates atomically flat terraces of Mn ML grown from the W step edges. Figure 1(c) shows an SP-STM image taken on an ML region of Mn/W(110) with a tip magnetized perpendicular to the sample surface. Bright and dark rows separated by an atomic distance along the [1$\bar{1}$0] direction indicate antiferromagnetic magnetization of the Mn [001] rows. The contrast vanishes periodically at the Mn rows whose magnetization directions are close to the in-plane direction (i.e., θ is close to 90°), indicating a spin-spiral structure.

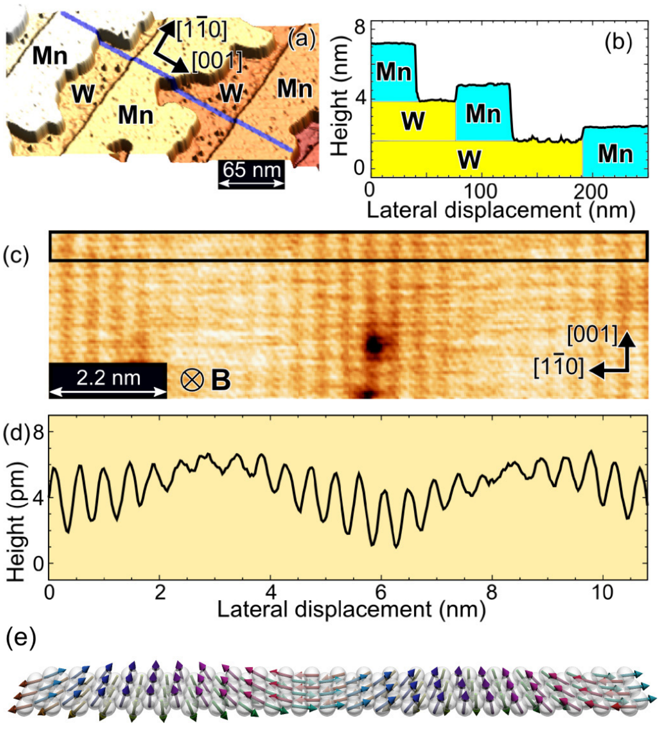

Fig. 1. (a) STM image of a Mn monolayer (ML) formed on a W(110) substrate. (b) Cross-sectional profile taken along the blue line in (a). (c) Spin-polarized STM image of 1 ML Mn/W(110) taken with an Fe-coated W tip magnetized perpendicular to the sample surface. (d) Cross-sectional profile averaged in the boxed area in (c). (e) schematic of the magnetic structure of ML Mn/W(110).

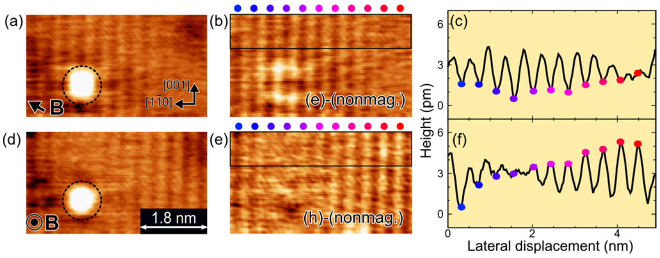

Fig. 2. (a, d) SP-STM images of 1 ML Mn/W(110) taken in the same area with an Fe-coated W tip magnetized in the in-plane (a) and out-of-plane directions (d) The direction of the applied magnetic field is shown by the arrows. (b, e) Images whose nonmagnetic contribution was subtracted from (a) and (d). (c, f) Cross-sectional profiles averaged in the boxed areas of (b, e). The same colored dots indicate the same atomic rows in the images of (b, c, e, f).

There are two possible types of spin spiral structure to explain the observed images; a cycloidal structure whose spins are rotating in the (001) plane and a helical one rotating in the (1$\bar{1}$0) plane. To determine the rotational type of the spin structure, SP-STM images are taken with a tip magnetized along the [001] direction. The obtained images showed suppressed magnetic contrast, indicating a cycloidal spin spiral structure. This result is consistent with the mechanism of the interfacial DMI, which only produces cycloidal spin spiral structures or Néel-type domain walls.

Then, in order to clarify the rotational sense of the cycloidal spin spiral structure, we performed SP-STM measurements with a spin-polarized tip magnetized in two orthogonal directions within the (001) plane. When we focus on every two adjacent spins, the magnetic contrast exhibits a sinusoidal variation. By changing the direction of the tip magnetization from parallel to perpendicular to the surface [*i.e.* from the leftward to the upward direction], we should observe +90° or -90° phase shifts in the sinusoidal profile depending on the rotational sense.

Figures 2(a, d) show SP-STM images taken in the same area with the tips magnetized in the directions shown in the figures. White clusters provide a proof that it is the same area. In order to extract the magnetic contrast, we subtracted the nonmagnetic contributions, which are derived by averaging two SP-STM images taken with the tips magnetized in opposite directions. Cross-sectional profiles shown in Figs. 2(c, f) indicate the direction of the phase shift is consistent with that expected for the left-handed spin spiral structure.

The domain walls in the Fe DL/W(110) were found as Néel-type domain walls with right-handed rotation, which can be explained by the consequence of the competition between ferromagnetic interaction ($\uparrow\uparrow$) and right-handed DMI ($\uparrow\rightarrow$). On the other hand, the left-handed rotation of Mn ML ($\uparrow\searrow\leftarrow\nearrow\downarrow$) is a consequence of the competition between antiferromagnetic interaction ($\uparrow\downarrow$) and right-handed DMI ($\uparrow\rightarrow$). We thus found the consistent role of the substrate on the polarity of DMI in the both cases.

Reference
[1] M. Haze, Y. Yoshida, and Y. Hasegawa, arXiv:1604.01123 (2016).

Authors
M. Haze, Y. Yoshida, and Y. Hasegawa

Nanocomposite Electrodes for Photoelectrochemical Water Splitting

Lippmaa Group

Photoelectrochemical water splitting can be used to harvest solar energy and produce hydrogen gas, which can be stored for later use in a fuel cell to generate electricity or used as a raw material for chemical synthesis. A major obstacle to wide-spread solar hydrogen production is the low efficiency of the energy conversion process due to large recombination losses in typical water-stable oxide semiconductors, such as titanates. In a typical oxide semiconductor, illustrated in Fig. 1a, a band bending region exists at the oxide-water interface, where electron-hole pairs are formed by light excitation and separated by the internal electric field. For an *n*-type semiconductor, photogenerated holes would be transported through a surface depletion layer to the surface, where the oxygen evolution reaction can take place. Hydrogen would be produced on a suitable counter electrode. However, only photocarriers formed within a few tens of nm of the surface can escape from the semiconductor and participate in water splitting, whereas photocarriers formed deeper in the semiconductor are rapidly lost to trapping and recombination. Considering the visible light absorption length, which is closer to micrometer scale in doped titanates, the fraction of incident light that can actually be converted to active photocarriers at the surface is on the order of a percent.

Various strategies exist for improving the charge extraction efficiency from oxide photoelectrodes. Besides a pure materials approach directed at finding more efficient semiconductors and doping schemes, it is also possible to design suitable nanoscale structures that improve charge collection by virtue of geometric effects. In our work, we have developed a method of growing noble-metal-doped titanate semiconductors where some of the noble metal segregates in the form of nanoscale pillars as illustrated in Fig. 1b.

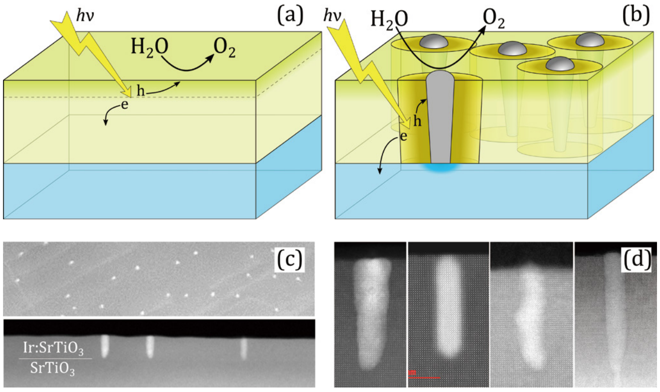

Fig. 1. (a) Operating principle of a photocatalytic energy conversion system where photogenerated charges are extracted only from a thin surface layer. (b) A nanopillar composite electrode where tubular Schottky junctions surrounding metal pillars extend the charge extraction region to the full depth of a thin film electrode. (c) Plan and cross-section STEM views of Ir metal nanopillars in a $Ir:SrTiO_3$ matrix, (d) Examples of (left-to-right) Ir, Pt, Pd, and Rh nanopillars grown in a $SrTiO_3$ matrix. The diameter of all pillars is 5 to 10 nm.

When the nanopillar consists of a high work function metal and the surrounding semiconductor is an *n*-type material, tubular Schottky junctions form around each pillar. The internal field of the Schottky junction ensures efficient charge separation and extraction throughout the thickness of the thin film photoelectrode, while the metal nanopillars provides a low-resistance charge extraction path to the film surface.

The formation of noble metal nanopillars is achieved by considering the kinetic and thermodynamic crystal growth parameters in a pulsed laser deposition process. For several noble metals, it is possible to find a balance between the oxidation rate of the metal and the growth rate of the crystal, where the average background oxygen pressure is low enough for metal segregation to occur at the initial growth stage of a film and the growth rate is balanced with the surface migration rate so that further segregated metal can form vertical pillar structures.

From the point of view of water splitting, the best starting material for the nanopillar composite photoelectrode growth is $Ir:SrTiO_3$. Homogeneously doped $Ir:SrTiO_3$ is an *n*-type semiconductor, while bulk iridium metal is a high workfunction material, ensuring that Schottky junctions form at Ir – $Ir:SrTiO_3$ interfaces. Additionally, Ir and IrO_2 are electrocatalysts that are known to promote the oxygen evolution reaction in water. The formation of segregated Ir metal inclusions in a $Ir:SrTiO_3$ film can be seen in scanning transmission electron microscope (STEM) plan and cross-section views in Fig. 1c. The cross-section image shows that the pillars do indeed nucleate at the $SrTiO_3$ substrate interface, and that approximately 10 nm wide pillars extend through the thickness of the film to the photoelectrode film surface. The spontaneous segregation behavior seen for Ir can be reproduced for a variety of noble metals. Although the particular growth parameters vary from metal to metal, nanopillar formation has been observed for Ir, Pt, Pd, and Rh (Fig. 1(d)).

Reference
[1] S. Kawasaki, R. Takahashi, T. Yamamoto, M. Kobayashi, H. Kumigashira, J. Yoshinobu, F. Komori, A. Kudo, and M. Lippmaa, Nature Commun. **7**, 11818 (2016).

Authors
S. Kawasaki, R. Takahashi, T. Yamamoto[a], M. Kobayashi[b], H. Kumigashira[b], J. Yoshinobu, F. Komori, A. Kudo[c], and M. Lippmaa
[a]Nagoya University
[b]Photon Factory, KEK
[c]Tokyo University of science

The Novel Magnetic and Valence Instabilities Tuned by Pressure in $YbNi_3Ga_9$

Uwatoko Group

In heavy fermion systems, non-Fermi liquid state and/or unconventional superconductivity often appear near a quantum critical point (QCP) where a second order phase transition is suppressed to zero temperature [1]. Therefore, pressure tuning of the ground state from a nonmagnetic state to a magnetic state or vice versa has attracted attention. The anomalous properties in the vicinity of QCP are described by the spin fluctuation theory, especially for most of Ce-based compounds, however, the unconventional critical behavior has been recently reported in several Yb-based heavy fermion compounds. Soon after, several theories have been proposed

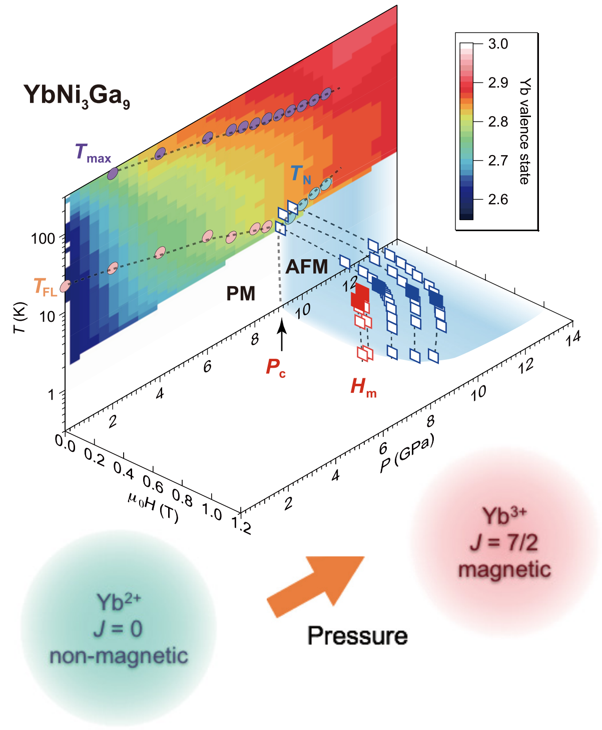

Fig. 1. Contour plot of the Yb valence in the temperature-pressure phase diagram of $YbNi_3Ga_9$. The transition and crossover temperatures are deduced from resistivity (circles) and ac magnetic susceptibility (squares) measurements. Here, closed squares below and above Pc indicate the CP and TCP, respectively. The dashed lines are guides to the eye.

to clarify the origin of the unconventional criticality, nevertheless, it remains an open question. Since the pressure variation of magnetism in Yb systems is accompanied by a valence change from the divalent to the trivalent state of Yb ions, direct observations of Yb valence toward the magnetic QCP is highly desirable. Here we show the realization of the pressure-induced valence crossover and the novel metamagnetic behavior possibly due to the valence instability near the magnetic quantum phase transition in intermediate valence $YbNi_3Ga_9$ [2,3].

Figure 1 shows the temperature-pressure-magnetic field phase diagram of $YbNi_3Ga_9$ together with a contour plot of the Yb valence value in the *T-P* plane. We have revealed a clear evolution of the Yb valence toward the magnetic trivalent state as well as the change from the nonmagnetic to the magnetic ground state with increasing pressure. The resulting phase diagram suggests that the occurrence of the pressure-induced first-order magnetic transition in $YbNi_3Ga_9$ is associated with enhanced valence fluctuations. This interpretation is consistent with the observations of a first-order metamagnetic transition below Pc, which is associated with the field-induced valence change from the mixed-valent state to the trivalent state with magnetic degrees of freedom. Our results suggest that the proximity to the critical end point of the first-order valence transition gives rise to the unconventional critical behavior in other Yb systems.

References
[1] P. Gegenwart, Q. Si, and F. Steglich, Nat. Phys. **4**, 186 (2008).
[2] S. Watanabe and K. Miyake, J. Phys. Condens. Matter **23**, 094217 (2011).
[3] T. Yamashita, R. Miyazaki, Y. Aoki, and S. Ohara, J. Phys. Soc. Jpn. **81**, 034705 (2012).
[4] K. Matsubayashi, T. Hirayama, T. Yamashita, S. Ohara, N. Kawamura, M. Mizumaki, N. Ishimatsu, S. Watanabe, K. Kitagawa, and Y. Uwatoko, Phys. Rev. Lett. **114**, 086401 (2015).

Authors
K. Matsubayashi[a], T. Hirayama, T. Yamashita[b], S. Ohara[b], N. Kawamura[c], M. Mizumaki[c], N. Ishimatsu[d], S. Watanabe[e], K. Kitagawa[f], and Y. Uwatoko
[a]University of Electro-Communications
[b]Nagoya Institute of Technology
[c]JASRI/SPring-8
[d]Hiroshima University
[e]Kyushu Institute of Technology
[f]University of Tokyo

Coupling of Two Quantum Hall States at Graphene Monolayer/Bilayer Boundary: Bulk-Edge Correspondence between Different Materials

Osada Group

The edge channel transport in the quantum Hall (QH) states has been extensively investigated in graphene systems. The subjects of most studies have been the p-n homo-junction of monolayer graphene (MLG) or bilayer graphene (BLG), since they were the first bipolar QH junctions between electron and hole QH states. The graphene p-n junctions are realized using the dual gate FET devices, in which an additional top-gate electrode partially covers MLG or BLG so as to control the carrier number and polarity of the covered part independently. In this case, both sides of the junction are the same material with the same band structure under different potential energy. The main issue was the mixing between the electron and hole QH edge channels propagating parallel along the junction in both sides.

Here, we consider another type of QH junctions in the graphene system, namely, the hetero-junction of MLG and BLG. In this case, the both sides of the junction have the same polarity (n-n or p-p junction), but they are different materials (MLG and BLG) with the different band structures: the low-energy band dispersion is the Dirac cone in MLG, but it shows the quadratic band touching in BLG. Under the perpendicular magnetic field **B**, these energy bands are quantized into the Landau levels (LLs), which have four-fold spin and valley degeneracies. The most characteristic feature is the appearance of the zero-energy LL resulting from the Berry phase of ± π and ± 2π around the band contact points in MLG and BLG, respectively. Note that the zero-energy LLs in MLG and BLG have different degeneracies; four-

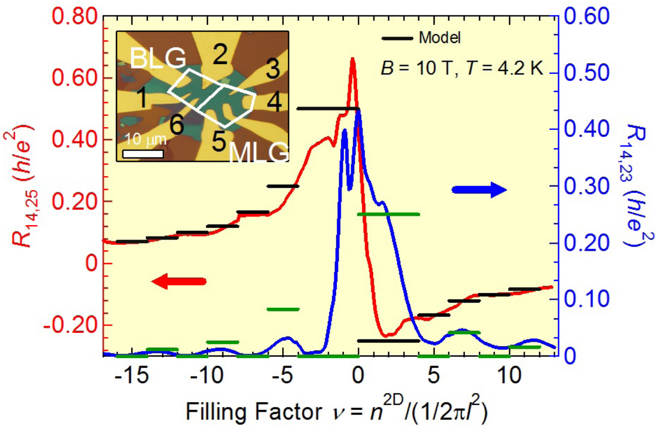

Fig. 1. Hall resistance $R_{14,25}$ and transverse resistance $R_{14,23}$ across the MLG/BLG junction. The horizontal bars indicate the quantized values assuming strong coupling limit. Inset: microscope image of the FET device.

fold in MLG but eight-fold in BLG in which both the n=0 and n=1 LLs degenerate to zero energy. This fact results in the different quantized values of the Hall conductivity; $\sigma_{xy} = N_1e^2/h = \pm(4N + 2)e^2/h$ in MLG and $\sigma_{xy} = N_2e^2/h = \pm(4N + 4)e^2/h$ in BLG ($N = 0, 1, 2, \cdots$). Here, N_1 and N_2 are the Chern numbers of the QH states in MLG and BLG, respectively. The spin or valley splitting is ignored.

In the present work, we have experimentally studied the QH edge transport across the MLG/BLG junction employing hexagonal boron nitride (h-BN) substrate, which remarkably improves sample quality, and we have clarified the edge channel configuration along the MLG/BLG junction. If the both sides of the junction is perfectly decoupled, there are $|N_1|$ and $|N_2|$ edge channels in MLG and BLG sides, respectively, so that they propagate in opposite direction along the junction. If finite coupling exists between both sides, they must show pair annihilation resulting in $|N_1| - n$ and $|N_2| - n$ channels at the boundary. At the strong coupling limit, $n = \min(|N_1|, |N_2|)$, $|N_2 - N_1|$ channels with the same direction remains at the boundary. These features are required from the bulk-edge correspondence at the boundary of two QH states, which basically originates from the charge conservation law. The coupling feature is not trivial since MLG and BLG have different crystal and band structures. Whereas electronic states in MLG consist of A and/or B site Wannier states, those in BLG mainly consist of A and/or B' site Wannier states. So, the envelope function is not continuous at the MLG/BLG boundary. The coupling depends on the connection of the true wave functions at the boundary.

Figure 1 shows the observed Hall resistance and transverse resistance across the MLG/BLG boundary of the FET device fabricated on h-BN substrate as functions of the filling factor, which is controlled by the back gate voltage. The carrier densities of the MLG and BLG parts are almost same, since the gate voltages of charge neutrality points coincide in both parts. The horizontal bars indicate the quantized values calculated from the Landauer-Büttiker formula assuming the strong coupling limit. The calculation well reproduces the observed result in the positive filling (n-type) region. Considering the BLG side shows imperfect QH effect in the negative filling (p-type) region in the present device, this agreement indicates that the coupling between two QH states at the boundary is so strong that the minimum number ($|N_2 - N_1|$) of edge channels survives at the boundary of MLG and BLG.

In the figure, we can see another remarkable feature around the zero filling. The transverse resistance shows fine dip structures. They are considered to reflect the degeneracy breaking of the zero-energy LL in MLG and BLG. Although no perfect splitting was observed in MLG or BLG in the present device, this result suggests the splitting of the edge channels along the boundary.

Authors

T. Osada, H. Nakase, F. Uehara, T. Taen, and K. Uchida

One-Third Magnetization Plateau with a Preceding Novel Phase in Volborthite

Hiroi, Kindo, Tokunaga and Takigawa Groups

We have synthesized high-quality single crystals of volborthite, a seemingly distorted kagome antiferromagnet, and carried out high-field magnetization measurements up to 74 T and ^{51}V NMR measurements up to 30 T. An extremely wide 1/3 magnetization plateau appears above 28 T and continues over 74 T at 1.4 K, which has not been observed in previous studies using polycrystalline samples (Fig. 1). NMR spectra reveal an incommensurate order (most likely a spin-density wave order) below 22 T and a simple spin structure in the plateau phase. Moreover, a novel intermediate phase called 'N' phase is found between 23 and 26 T, where the magnetization varies linearly with magnetic field and the NMR spectra indicate an inhomogeneous distribution of the internal magnetic field (Fig. 2). This sequence of phases in

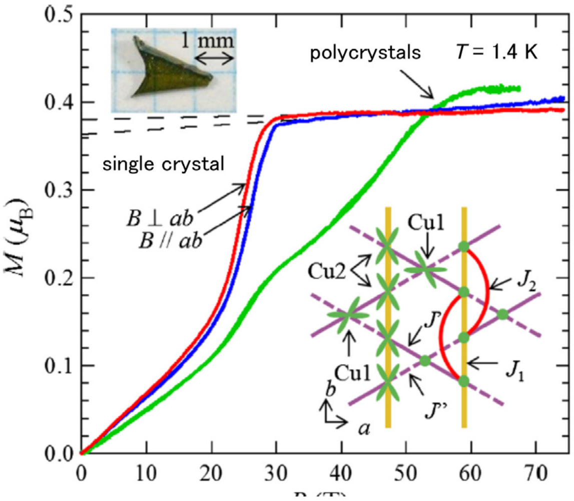

Fig. 1. Magnetization curves of volborthite measured at 1.4 K on two piles of single crystals in magnetic fields perpendicular (red line) and parallel (blue line) to the *ab* plane, and on a polycrystalline sample (green line). Shown also are a typical single crystal of volborthite (upper left) and the arrangement of Cu d_{x2-y2} orbitals projected onto the *ab* plane in the low-temperature $P2_1/a$ structure (lower right). J_1 and J_2 represent the NN and NNN interactions in the Cu2 spin chains, respectively. J' and J'' represent the NN interactions between Cu1 and Cu2 spins.

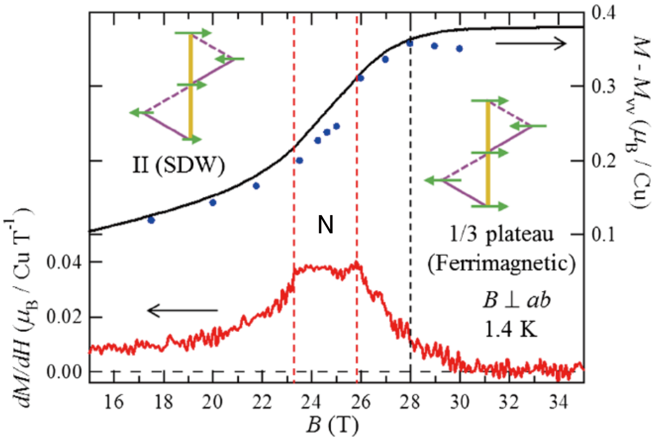

Fig. 2. Magnetization curve of single crystals (top, black line) and its field derivative (bottom) in $B \perp ab$ at 1.4 K after the subtraction of the Van Vleck paramagnetic magnetization (M_{VV}). Magnetization deduced from the center of the gravity of the NMR spectra is also plotted (top, blue circles). Phase 'N' with a linear field dependence of magnetization exists between phase II (SDW) and the 1/3 plateau state.

volborthite bears a striking similarity to those of frustrated spin chains with a ferromagnetic nearest-neighbor coupling J_1 competing with an antiferromagnetic next-nearest-neighbor coupling J_2. This analogy suggests that the N phase is related to a spin nematic order that is expected to appear in "frustrated" ferromagnets.

How do we understand the appearance of this series of magnetic phases in volborthite under magnetic fields? Among the various possible spin models for volborthite, we now consider a $J_1 - J_2 - J' - J''$ model on the distorted kagome net (see Fig. 1) as the most likely. Using DFT + U calculations, Janson and his coworkers evaluated the magnetic interactions and found that J'' is the strongest antiferromagnetic coupling, which results in a coupled trimer model [2]. In this model, the 1/3 plateau phase pertains to polarized magnetic trimers formed by J'' bonds. Their theoretical considerations also predict the presence of a spin nematic phase just before the 1/3 saturation, which seems to correspond to our N phase.

References
[1] H. Ishikawa, M. Yoshida, K. Nawa, M. Jeong, S. Krämer, M. Horvatić, C. Berthier, M. Takigawa, M. Akaki, A. Miyake, M. Tokunaga, K. Kindo, J. Yamaura, Y. Okamoto, and Z. Hiroi, Phys. Rev. Lett. **114**, 227202 (2015).
[2] O. Janson, S. Furukawa, T. Momoi, P. Sindzingre, J. Richter, and K. Held, arXiv:1509.07333.

Authors
H. Ishikawa, M. Yoshida, K. Nawa, M. Jeong[a], S. Krämer[a], M. Horvatić[a], C. Berthier[a], M. Takigawa, M. Akaki, A. Miyake, M. Tokunaga, K. Kindo, J. Yamaura, Y. Okamoto, and Z. Hiroi
[a]LNCMI-CNRS, Grenoble

SU(N) Heisenberg Model with Multicolumn Representations

Kawashima Group

Realization of quantum spin liquid in short-range coupling models has been a popular research target in condensed-matter physics for several decades. One approach to obtain a spin liquid state is to consider a Hamiltonian with higher symmetry, which increases quantum fluctuations. Read and Sachdev generalized the antiferromagnetic Heisenberg into SU(N) symmetry [2]. Based on the $1/N$ expansion they showed that the ground state of the model with sufficiently large N is a valence-bond-solid (VBS) ordering breaking the lattice rotational or the translational symmetry spontaneously. Recently, in the context of the deconfined quantum criticality [3], their theory attracts renewed attention. In particular, the existence of an intermediate state, which might be a spin-liquid state, was discussed near the boundary of Néel and VBS [4,5].

With the famous example of the Haldane gap states, it is now well-known that the nature of the ground state can strongly depend on the representation of the symmetry group even if the symmetry itself is the same. It also applies to the present problem. We consider SU(N) Heisenberg model with the representation of the Young diagram with a single row and n columns. Previously, it was found [4,5] that the Néel state for small N switches to the VBS state for large N without an intermediate spin liquid state. In the case of n = 2, 3, 4, however, though the Néel order disappears at some value of N, no evidence of VBS order has been found in QMC calculation for the L×L square lattice up to L = 32 [5]. At first sight, this result may appear to suggest an intermediate phase between the Néel phase and the VBS phases. In the present work [1], we investigate this problem to clarify whether the intermediate phase exists or not.

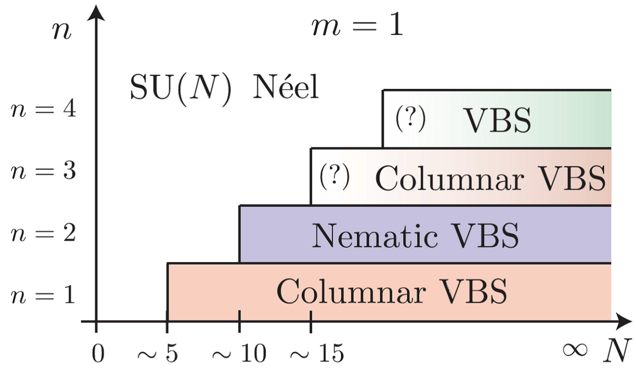

Fig. 1. Schematic phase diagram of the SU(N) Heisenberg model on the square lattice with single-row (m = 1) representations. The phase boundaries for the case of n = 2,3 are determined in the present study. In the case of n = 3,4, we do not see clear evidence of the spontaneous VBS order in the vicinity of the phase boundaries for finite-size QMC simulations.

First, we examine the case of n = 2. In Fig. 2, we show the Binder parameter of the VBS order parameter for various N and L. The Binder parameter should be 1 when the corresponding order exists and 0 otherwise. From the figure, we see that the VBS order is absent for N = 9 while it exists for N = 11. While the case N = 10 may seem marginal at the first sight, it is approaching the value 1 as can be seen in the inset. From these observations, we conclude that in the case of n = 2 the ground state is the Néel state for $N \leq 9$, while it is the nematic VBS state for $N \geq 10$. There is no intermediate phase.

For n = 3 and 4, the problem is harder. In the case of n = 3, while the system size dependence of the Néel order parameter shows that the Néel states end at N = 14, no clear VBS order can be seen in our calculation up to L = 128. To see if this can be regarded as an evidence of the intermediate spin liquid state, we re-examine the prediction of the large-N theory [2], and we find a correspondence between the two cases: (n,N) = (2,10) and (3,15). When the order is small, even if it is finite, the numerical estimate shows apparent $1/L$ decay for small L regime, and eventually deviates from it. From the known size dependence of the order parameter for the (2,10) case and the correspondence between the two cases, we estimate the cross-over system size at which the size dependence starts to deviate from $1/L$ behavior in the (3,15) case. It turns out that this cross-over size is around L = 400, indicating that the order is too small to detect even

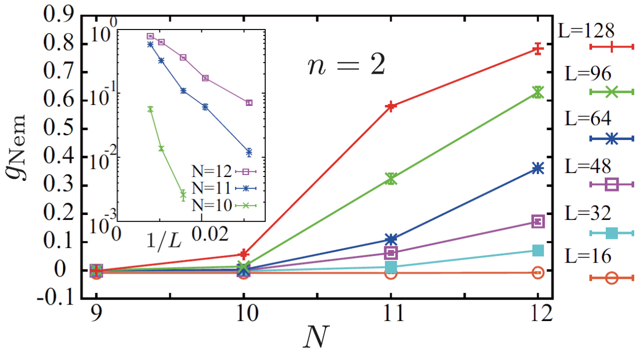

Fig. 2. The Binder cumulant of the nematic order parameter for the model with n = 2 for 16 ≤ L ≤ 128. The inset shows size dependence of the Binder cumulant for N = 10, 11 and 12 in the semi-log scale. The error bars represent the standard errors.

if it exists as the $1/N$ theory predicts. The situation is similar for the $n = 4$ case.

To summarize, none of the existing evidence contradict to the absence of the intermediate spin liquid phase, and the absence is confirmed in the $n = 2$ case while direct confirmation is still missing for larger n.

References

[1] T. Okubo, K. Harada, J. Lou, and N. Kawashima, Phys. Rev. B **92**, 134404 (2015)
[2] N. Read and S. Sachdev, Phys. Rev. B **42**, 4568 (1990); N. Read and S. Sachdev, Nucl. Phys. B **316**, 609 (1989).
[3] T. Senthil, A. Vishwanath, L. Balents, S. Sachdev, and M. P. A. Fisher, Science **303**, 1490 (2004).
[4] K. Harada, N. Kawashima, and M. Troyer, Phys. Rev. Lett. **90,** 117203 (2003).
[5] N. Kawashima and Y. Tanabe, Phys. Rev. Lett. **98**, 057202 (2007).

Authors

T. Okubo, K. Harada, J. Lou, and N. Kawashima

Membrane Tubulation and Polyhedral Vesicle Formation Induced by Banana-Shaped Proteins

Noguchi Group

In living cells, membrane morphology is regulated by various proteins. Many membrane reshaping proteins contain a Bin/Amphiphysin/Rvs (BAR) domain, which consists of a banana-shaped rod. The BAR domain bends the biomembrane along the rod axis and the features of this anisotropic bending have recently been studied. We study as to how such a local anisotropic curvature induces effective interaction between proteins and changes the global shape of vesicles and membrane tubes using meshless membrane simulations. The proteins are modeled as banana-shaped rods strongly adhered to the membrane.

Our study revealed that the rods assemble via two continuous directional phase separations in membrane tubes and vesicles unlike a conventional two-dimensional phase separation [1]. As the rod curvature increases, the rods assemble along the azimuthal direction and subsequently along the longitudinal direction accompanied by shape transformation of the membrane tube. In the vesicle, in addition to these two assembly processes, further increase in the rod curvature induces tubular scaffold formation. We also found that the polyhedral vesicles and polygonal tubes are stabilized at high rod densities [2]. The discrete shape transition between triangular and buckled discoidal tubes and between polyhedral shapes are obtained. As line tension of the membrane edge is reduced, the protein adhesion induces membrane rupture leading to high-genus vesicle formation and vesicle inversion [3]. These shape transformations and assemblies are not obtained by isotropic inclusions.

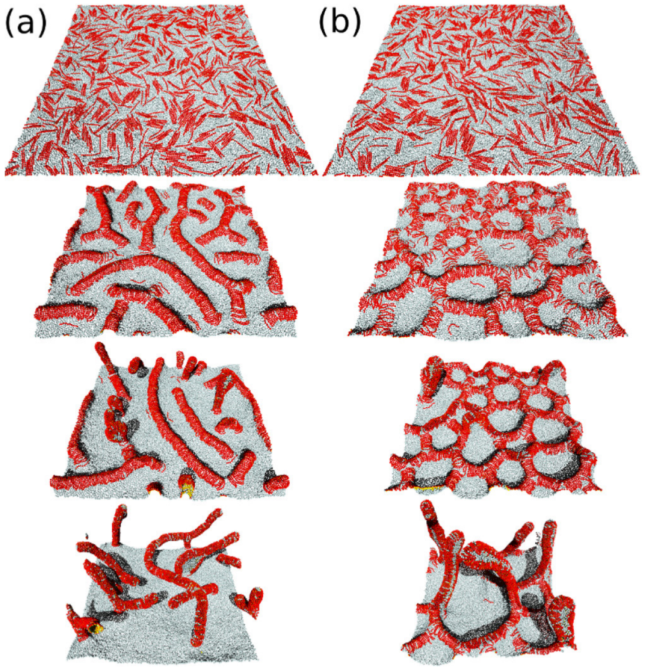

Fig. 1. Sequential snapshots of tabulation from a flat membrane induced by protein rods. (a) Positive perpendicular rod curvature. (b) Negative perpendicular rod curvature.

We also studied the effects of the spontaneous (side) curvature perpendicular to the rod, which can be generated by protein–protein and membrane–protein interactions [4]. We revealed that the perpendicular curvature can drastically alter the tubulation dynamics from a flat membrane at high protein density whereas no significant difference is obtained at low density. A percolated network is intermediately formed depending on the perpendicular curvature. This network suppresses tubule protrusion. Thus, this kinetic trap makes tubule formation significantly slower. The stability of network structures can be explained by a simple geometric model. Positive surface tensions and vesicle membrane curvature can stabilize this network structure by suppressing the tubulation. It is known that tubulation dynamics can be different even for proteins consisting of the same BAR domains. Our finding suggests that the interactions between the rest parts of the proteins can give significant effects.

References

[1] H. Noguchi, EPL **108**, 48001 (2014).
[2] H. Noguchi, J. Chem. Phys. **143**, 243109 (2015).
[3] H. Noguchi, Phys. Rev. E to be published (arXiv:1602.04569).
[4] H. Noguchi, Sci. Rep. **6**, 20935 (2016).

Author

H. Noguchi

Formation and Structure of Carbon Dioxide Glass

Yamamuro Group

Glass can be recognized as the ‘fourth state of matter’ following gas, liquid, and solid. Compared with the conventional three states, glass is more mysterious and leaves many unsolved problems from the viewpoint of physics. One of the most important problems is the ‘basic structure of glasses’. Is it similar to the local structure of the corresponding crystal or characteristic of the glass such as an icosahedral cluster? This problem is recently remarked more and more as it has been understood that the mechanism of the glass transition is deeply associated with the local and/or medium-range structures of glasses.

For metallic glasses, a bulk glass of tantalum (Ta) was experimentally obtained recently [1] and its structure was confirmed to be an aggregate of icosahedral clusters from the molecular dynamics simulation [2]. On the other hand, for simple molecular glasses which additionally have an orientational degree of freedom, there have been few structural works since their glass transition temperatures are very low

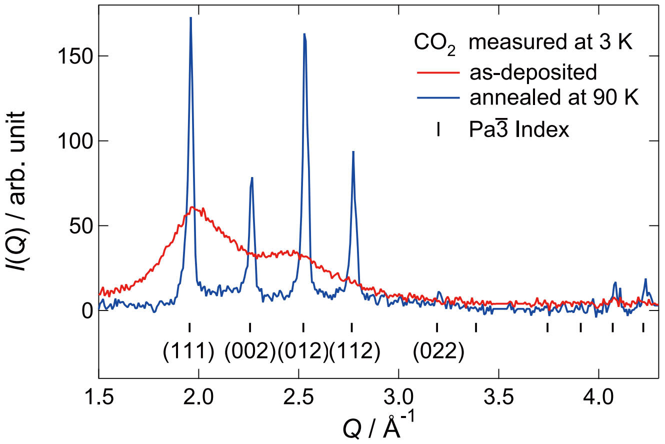

Fig. 1. X-ray diffraction patterns of the vapor-deposited CO_2 measured at 3 K. The red and blue curves represent the data of the as-deposited and 90 K-annealed samples, respectively. The tick marks with Miller indices show the peak positions calculated from the crystalline data [7] with a space group Pa-3.

and they are readily crystallized on cooling. Our group has formed several simple molecular glasses by means of a vapor deposition (VD) method, and investigated their thermal and structural properties [3-6]. The vapor-deposition is the most rapid cooling method, in which molecules at a gas state are condensed on a cold substrate. The cooling rate is estimated to be higher than 10^7 Ks^{-1}. In this work, we have tried to form a CO_2 glass, which has never been vitrified.

The red curve in Fig. 1 shows the X-ray diffraction pattern of the as-deposited sample measured at 3 K. This data clearly exhibits a typical halo pattern characteristic of amorphous structures, indicating that the amorphous form of CO_2 was successfully prepared by the VD method. We would like to emphasize that this is the simplest molecular glass ever realized. On heating the VD sample, many Bragg peaks, which are a direct evidence of crystallization, appeared at 25 K. To obtain the complete crystalline state, the sample was annealed at 90 K for 5 min and then cooled again to 3 K. The blue curve in Fig. 1 presents the diffraction pattern of the annealed sample exhibiting sharp Bragg peaks. The peak positions are well reproduced in terms of the reported crystal structure (space group Pa-3) [7] as shown by the tick marks in Fig. 1.

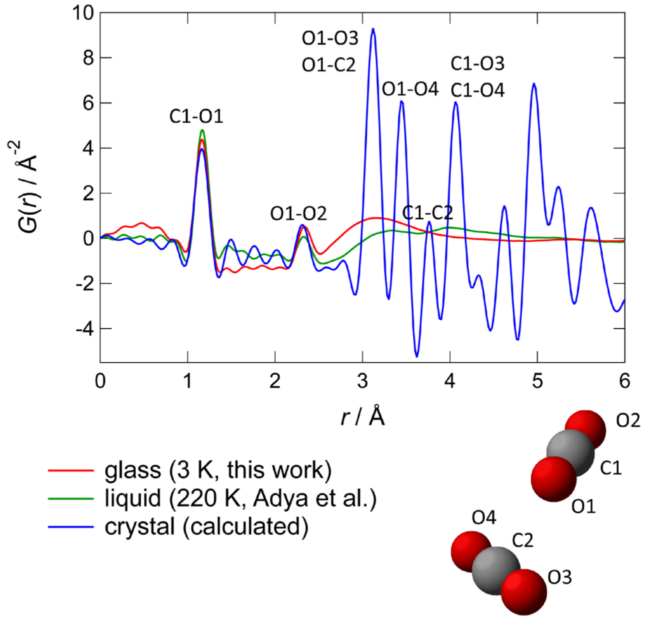

Fig. 2. Pair distribution functions for glassy, liquid, and crystalline CO_2. The nearest neighbor configuration in crystalline CO_2 is schematically shown below the graph. The label corresponding to each atomic correlation is depicted in the graph.

Figure 2 shows the pair distribution functions *G*(*r*) of glassy, liquid, and crystalline CO_2. The former two were obtained by the Fourier transformation of the observed diffraction data and previous data on liquid CO_2 at 220 K and 0.85 MPa [8]. The *G*(*r*) of crystalline CO_2 was calculated from the crystal data [7]. The configuration of the neighboring two CO_2 molecules in the crystalline state is also depicted in Fig. 2. The peaks around 1.15 Å and 2.3 Å, which are common in all states, correspond to the C-O and O-O correlations within a molecule, respectively. The *G*(*r*) of the glassy sample exhibits a peak around 3.1 Å, while that of the liquid sample broader peaks around 3.3 Å and 4.0 Å. It is noteworthy that the peak position of the glassy sample (3.1 Å) coincides with the shortest intermolecular correlation (O1-C2, O1-O3) in the crystalline state. This indicates that the glassy CO_2 has a strong intermolecular correlation which is similar to that in crystalline CO_2. This is the first experimental evidence for the basic structure of glasses.

References

[1] L. Zhong *et al*., Nature **512**, 177 (2014).
[2] J. C. Zhang *et al*., Mater. Des. **77**, 1 (2015).
[3] O. Yamamuro *et al*., Europhys. Lett. **63**, 368 (2003).
[4] O. Yamamuro *et al*., J. Chem. Phys. **115**, 9808 (2001).
[5] O. Yamamuro *et al*., J. Chem. Phys. **106**, 2997 (1997).
[6] S. Tatsumi *et al*., Phys. Rev. Lett. **109**, 045701 (2012).
[7] A. Simon *et al*., Acta. Cryst. B**36**, 2750 (1980).
[8] A. K. Adya *et al*., Mol. Phys. **77**, 1217 (1992).

Authors

Y. Mizuno, M. Kofu, and O. Yamamuro

Magnetic Model in Multiferroic $NdFe_3(BO_3)_4$ Investigated by Inelastic Neutron Scattering

Masuda Group

Symmetry breaking of time reversal and space inversion allows spontaneous order both in magnetism and dielectricity. The enhanced simultaneous order, multiferroics [1], has been extensively studied since the discovery of its experimental realization in the perovskite manganite $TbMnO_3$ [2]. The microscopic consideration of electronic states taking into account a spin-orbit interaction and symmetry of crystals reveals the relationship between the structures of spin and polarization. So far, in many multiferroic materials, the complex spin structure of the 3*d* transition metal ions has been focused in relation with induced electric polarizations. On the other hand, existence of an interaction between 4*f* and 3*d* ions (*f*-*d* coupling) and its importance on the multiferroic structure has not been in the spotlight. In this context, an easy-plane type antiferromagnet $NdFe_3(^{11}BO_3)_4$ provides a simple and interesting playground in which Nd and Fe moments are simultaneously ordered thorough the *f*-*d* coupling and the polarizations are simply described by a rank two tensor of local magnetic operators. Recently we performed inelastic neutron scattering (INS) measurements on single crystals of hexagonal $NdFe_3(^{11}BO_3)_4$ to explore the magnetic excitations, to establish the underlying Hamiltonian, and to reveal the detailed nature of hybridization between the 4*f* and 3*d* magnetism and its relation to

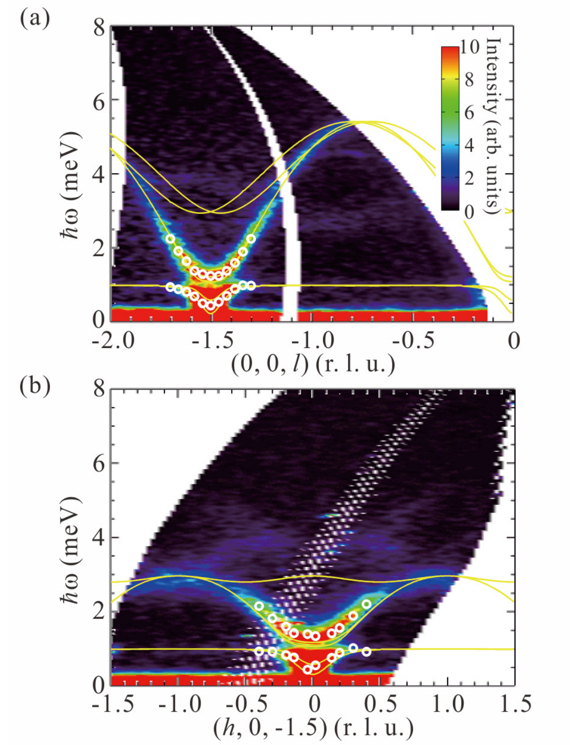

Fig. 1. Inelastic neutron scattering spectra obtained using HRC, along the (a) c^* and (b) a^* directions. The curves are the calculated spin-wave dispersions.

the multiferroic structure by using state-of-the-art neutron spectrometer HRC [3].

The INS spectra projected onto $\hbar\omega$-c^* and $\hbar\omega$ -a^* plane are shown in Figs. 1(a) and 1(b). We clearly observed the spin waves of the Fe^{3+} moments around AF zone center at $\boldsymbol{q}$ = (0,0, −1.5), and the flat excitation at about 1.0 meV from the crystal field of Nd^{3+} ion. Overall spectra are reasonably reproduced by spin-wave calculation including spin interaction in the framework of weakly coupled Fe^{3+} chains, f-d coupling, and single-ion anisotropy derived from the Nd^{3+} crystal field. Hybridization between the 4 f and 3d magnetism is probed as the anticrossing of the Nd- and Fe-excitations. The in-plane anisotropy gap at the AF zone center is explained solely by the crystal field of the Nd^{3+} ion in the quantitative level. The magnetic anisotropy of the Fe^{3+} ion allowed in the crystal structure is found to be negligibly small after the consideration on dipole-dipole interaction, single ion anisotropy, and spin nematic interaction as the origin of the in-plane anisotropy. Combination of the measurements and calculations revealed that the hybridization between 4 f and 3d magnetism propagates the local magnetic anisotropy of the Nd^{3+} ion to the Fe^{3+} network, resulting in the bulk magnetic structure. In the multiferroics of the spin-dependent metal-ligand hybridization type, the local magnetic anisotropy controls the electric polarization, meaning that the local symmetry of the rare-earth ion is a driving force for the nonlocal multiferroicity in $NdFe_3(^{11}BO_3)_4$.

References

[1] W. Eerenstein, N. D. Mathur, and J. F. Scott, Nature (London) **442**, 759 (2006).
[2] T. Kimura, T. Goto, H. Shintani, K. Ishizaka, T. Arima, and Y. Tokura, Nature **426**, 55 (2003).
[3] S. Hayashida, M. Soda, S. Itoh, T. Yokoo, K. Ohgushi, D. Kawana, H. M. Ronnow, and T. Masuda, Phys. Rev. B **92**, 054402 (2015).

Authors

S. Hayashida, M. Soda, S. Itoh, T. Yokoo, K. Ohgushi, D. Kawana, H. M. Ronnow, and T. Masuda

Magnetic Fields up to 370 T Revealed Aharonov-Bohm Exciton Splitting in Carbon Nanotubes

Takeyama Group

Rolled graphene with a certain chirality vector (n, m) forms a single-walled carbon nanotube (SWNT), possessing different electrical properties depending on the chirality, changing from semiconductors to metals. The penetration of magnetic flux quanta into a SWNT breaks the time-reversal symmetry of the electronic states, and the effect is known as the Aharonov-Bohm (A-B) effect. The quasi-one dimensionality of SWNTs enhances the effects of exciton as well as electron correlation in the band-edge optical properties. Owing to the A-B effect, a magnetic flux penetrating the cross section of a SWNT induces the valley splitting between the K and K' points in the Brillouin zone, along with a mixing of the exciton wave functions, and eventually the bright exciton and its dark counter part are converted into two independent bright K and K' point excitons in a limit of strong magnetic fields. The $k \cdot p$ theory by Ando [1], has predicted magnetic field evolution of the K and K' point exciton absorption spectra differently, depending on the relative energy-level ordering of the bright and dark band-edge excitons.

We have observed a discernible linear peak splitting of the K and K' point exciton absorption spectra of SWNTs in magagauss magnetic fields above the field where the exciton wave function mixing is over. Highly-selected (6,5) single-chirality SWNTs synthesized by a single-surfactant multicolumn-gel-chromatography method [2] were further processed to highly alignment of the tubes to yield average 29 degrees alignment by a polyvinyl alcohol thin film stretching.

The thin stretched film sample was set inside of the flux-compression coil with input and output optical fibers in such a way that magnetic field was oriented along the film stretching direction (the Voigt configuration). The transmission light was detected by a streak camera equipped with a CCD camera. A streak image of absorption spectra was obtained in magnetic fields up to around 370 T generated by

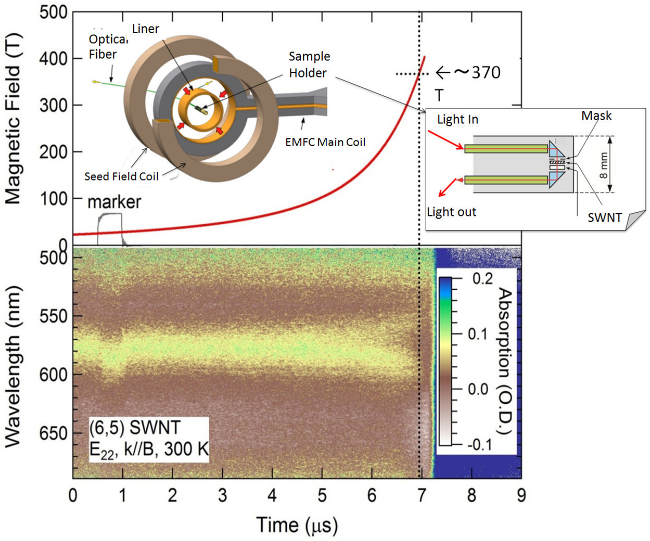

Fig. 1. A streak 2-dimensional image of the E_{22} second sub-band absorption of (6,5) SWNTs with a signal of magnetic field measured at 300 K. The inset illustrates sample setting with optical fibers inside a EMFC coil.

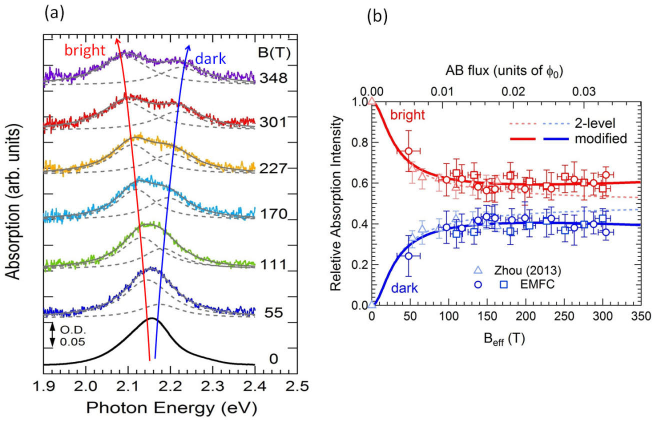

Fig. 2. (a) The band-edge absorption spectra at each magnetic field obtained from Fig.1. (b) The absorption intensity evolution in magnetic fields. The solid lines are the results of fitting using a two-energy level model (dotted line) modified with a linear *B* term. Triangles are obtained by the single-turn coil ultra-high magnetic field generator in magnetic fields up to 160 T.

the electro-magnetic flux compression ultra-high magnetic field generator, and the result was shown for the E_{22} second sub-band transition of a sample of (6,5) chirality SWNTs in Fig. 1. Absorption peak centered at 575 nm showed clearly a splitting when the magnetic field exceeds 170 T. The absorption spectra were plotted at each magnetic field strength from Fig. 1, and plotted in Fig. 2(a) with those of Lorentzian de-convolution spectral lines (dotted line). The peak energy splits linearly with magnetic field with the splitting $\Delta_{ab} = \mu B_{\mathrm{eff}}$ (where, μ: exciton splitting coefficient = 0.5, $B_{\mathrm{eff}} = B\cos(29)$, and B is the strength of an external magnetic field) above 150 T. The integrated intensity of the absorption spectrum of each *K* and *K*' splitting component exhibited linear magnetic field dependence above 200 T, but with their intensity recovers to that of the original peak, respectively, as seen in Fig. 2(b). Simple two-energy level mixing model does not hold anymore [3], but should be modified with a linear *B* term. All these phenomena evolve quite similarly with those presented by the theory of T. Ando [1]. We have figured out that the linear term is correlated to the environmental static dielectric constant, and found that the value amounts to 50, which arises likely from residual water molecules in hydrophilic PVA film [4].

References

[1] T. Ando, J. Phys. Soc. Jpn. **75**, 024707 (2006).
[2] H. Liu *et al*., Nat. Commun. **2**, 309 (2011).
[3] W. Zhou, D. Nakamura, H. Liu, H. Kataura, and S. Takeyama, Scientific Reports **4**, 6999 (2014).
[4] D. Nakamura, T. Sasaki, W. Zhou, H. Liu, H. Kataura, and S. Takeyama, Phys. Rev. B **91**,235427 (2015).

Authors

D. Nakamura and S. Takeyama

Generation of Flat-Top Pulsed Magnetic Fields at ISSP

Kindo Group

Pulsed magnetic fields are commonly used where extremely strong magnetic fields are required. However, pulsed magnetic fields only persist for a short period of time which makes a scientific research difficult to conduct. The most commonly used pulsed field is driven by a capacitor bank and its field duration is typically from 1 to 100 milliseconds. Because of the extremely short timescale, most of experiments are difficult to perform, and only selected measurement techniques (such as magnetization and electronic resistivity) have been applied in pulsed magnetic fields. To solve this problem, some facilities in foreign countries start to utilize a flywheel generator and produces a "long" pulsed magnetic field that has ~1 second pulsed field duration. In 2008, International MegaGauss Science Laboratory at ISSP also installed the 51.3 MW DC flywheel generator and successfully produced long pulsed magnetic fields. The use of flywheel generator also enables us to generate a flat-top pulsed magnetic field (FTPMF) which has a constant field region around the maximum field. Since the FTPMF is the most demanding field profile for performing a precise experiment, we are now trying to generate highly stabilized FTPMFs with a homemade feedback controller. In this report, we would shortly describe our recent achievement of generating a FTPMF and its application to a scientific research.

Our homemade feedback controller consists of a FPGA (field programmable gate array) devise and a mini-coil circuit and is used in conjunction with a commonly used pulsed magnet[1]. The mini-coil is inserted into a pulsed magnet and modifies the original pulsed field profile to obtain a FTPMF. In Fig. 1 and 2, we show the generated field profiles of FTPMFs (60.64 ± 0.005 T for 2 ms and 35.5 ± 0.01 T for 90 ms) which are obtained with the mid-pulsed magnet (36 ms, 60 T) and the long-pulsed magnet (1.2 s, 36 T), respectively. In both cases, an extremely high field stability (±0.005~0.01 T) were obtained with feedback control of magnetic fields (see black curves). Since there is currently no alternative way to produce a FTPMF with high stability of the magnetic field, these FTPMFs can be used for improving the resolution of data with signal averaging or for performing a slow measurement (such as NMR and specific heat) at unprecedented high magnetic fields. The FTPMF shown in Fig. 2 is already utilized to perform a collaboration research and some specific heat data have been obtained. As shown as the green curve in Fig. 2, the temperature of the sample was recorded as a function of time. During the stabilized FTPMF, we applied heat pulses (ΔQ) to the sample and observed the resultant temperature jumps (ΔT). From each

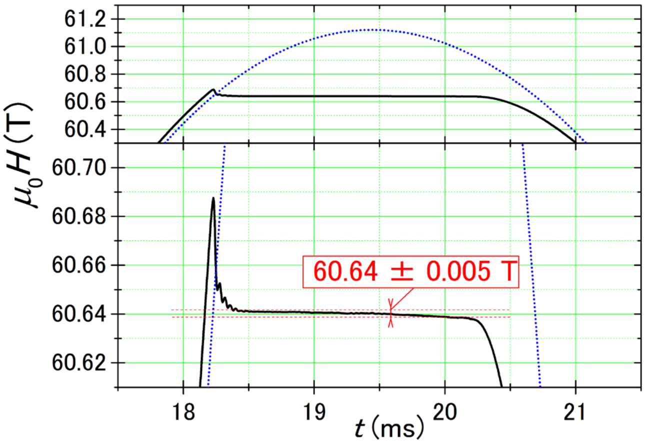

Fig. 1. Flattop pulsed field profile generated by 60 T user-coil and 1.2 T mini-coil. The user-coil and mini-coil were driven by the conventional capacitance banks and the lead batteries, respectively. The magnetic field generated by mini-coil is regulated by a homemade feedback controller and makes the pulsed field profile flat on the top of pulsed fields. The black (blue) curve is obtained with (without) the feedback control.

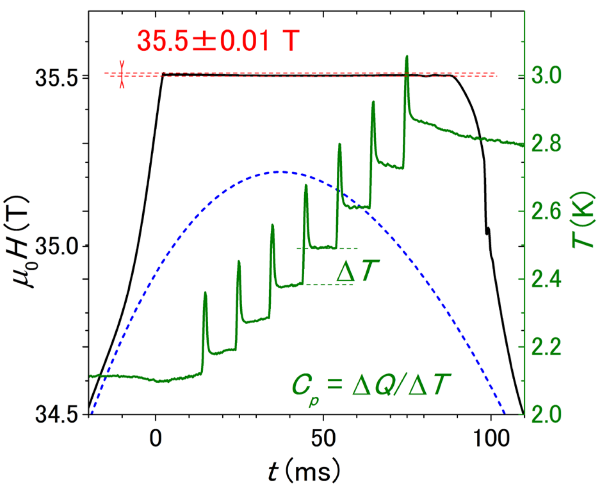

Fig. 2. Flattop pulsed field profile obtained with 36 T long pulsed magnet and 1.1 T mini-coil, which were driven by the DC flywheel generator and the lead batteries, respectively. The black curve indicates a field profile of a stabilized FTPMF. The field profile generated only with 36 T long pulsed magnet (no feedback control) is shown by a blue dashed curve. The temperature (green curve) and heat power (not shown) were recorded for the specific heat measurement.

temperature jump, we successfully estimated the specific heat ($C_p = \Delta Q/\Delta T$) and obtained several specific heat data points from a single pulse of magnetic fields.

We are planning to extend the time duration of FTPMF by a factor of 2 to 3 in 2016. Adding to the specific heat measurement, the generation of a highly stabilized FTPMF may open the way to perform a precise measurement that has never been possible in pulsed magnetic fields.

Reference

[1] Y. Kohama and K. Kindo, Rev. Sci. Instrum. **86**, 104701 (2015).

Authors

Y. Kohama and K. Kindo

Magnetic Field Induced Polar Phase in the Chiral Magnet CsCuCl$_3$

Tokunaga Group

Among the triangular lattice antiferromagnets, hexagonal CsCuCl$_3$ has been studied for a long time because of its interesting crystal and magnetic structures, and magnetic field induced phenomena. Owing to the Jahn-Teller distortion, Cu chains along the *c* axis are displaced helically in the triangular *ab* plane and form helices with a six-ion periodicity. This distortion makes the Dzyaloshinskii-Moriya (DM) interaction active with the *D* vector pointing to the *c* axis. The $S = 1/2$ spins of Cu^{2+} ions are ferromagnetically and antiferromagnetically coupled within and between the helical chains, respectively. The competition of ferromagnetic exchange and DM interaction induces the helical spin configuration with an incommensurate (IC) magnetic propagation vector (1/3, 1/3, $\delta = 0.085$) below $T_N \sim 10.7$ K at zero field, in which spins lie on the triangular *ab* plane [1]. The magnetic field (H) applied normal to the *c* axis induces a plateau-like behavior in magnetization between 10.5 and 14.5 T before the spin saturation at 30 T, while for $H // c$ axis magnetization shows a jump at 12.5 T [2]. With increasing $H \perp c$, the IC wave number δ decreases to ~ 0.05 at the beginning of the plateau [IC1 phase in Fig. 1(a)], remains constant in the plateau region (IC3), and decreases to zero on entering a commensurate (C) phase [3]. Using a pulse magnet developed at ISSP, we discovered a new multiferroic (MF) phase and discussed the origin of the emergence of the electric polarization in the chiral magnet CsCuCl$_3$ [4].

Figure 1(b) represents the magnetization (M) of CsCuCl$_3$ at 1.4 K as a function of H applied along the *a*, *b** and *c* axes, where *b** is perpendicular to the *ac* plane. In addition to the reported anomalies, we newly observe a jump of M above the plateau region for $H // a$ or *b** axis, which is clearly seen as a sharp peak in the dM/dH curve in Fig. 1(c). This field corresponds to the phase transition to the C phase. The most intriguing observation is that the electric polarization along the *a* axis (P_a) becomes finite just above the IC3 phase and disappears in the C phase for $H \parallel b^*$, as shown in Fig. 1(c). The induced P is as small as ~ 0.25 μC/m^2. Figure 1(a) is the magnetoelectric phase diagram for the H_{b^*}-T plane. The MF phase is located at H between the upper bound of the M plateau and the lower bound of the C phase. According to a classical calculation [5], spins in each chain are expected to form a chiral soliton lattice in this field region. Observation of higher harmonics in neutron diffraction supports this theoretical prediction [6]. The chiral soliton lattice state comes to attract considerable attention after its discovery in metallic CrNb$_3$S$_6$ that belongs to the same point group (622) as that of CsCuCl$_3$ [7]. The present insulating material exhibits finite electric polarization in the relevant field region. The helical arrangement of Cu ions results in finite local electric polarization normal to the *c* axis through the spin current mechanism even in the proper screw-type spin order because of the non-zero $\boldsymbol{e}_{ij} \times (\boldsymbol{S}_i \times \boldsymbol{S}_j)$ term as shown in Fig. 1(d) [4]. This local polarization will be cancelled out if the helical spin arrangement is incommensurate with the lattice period. In the soliton lattice state, however, distance

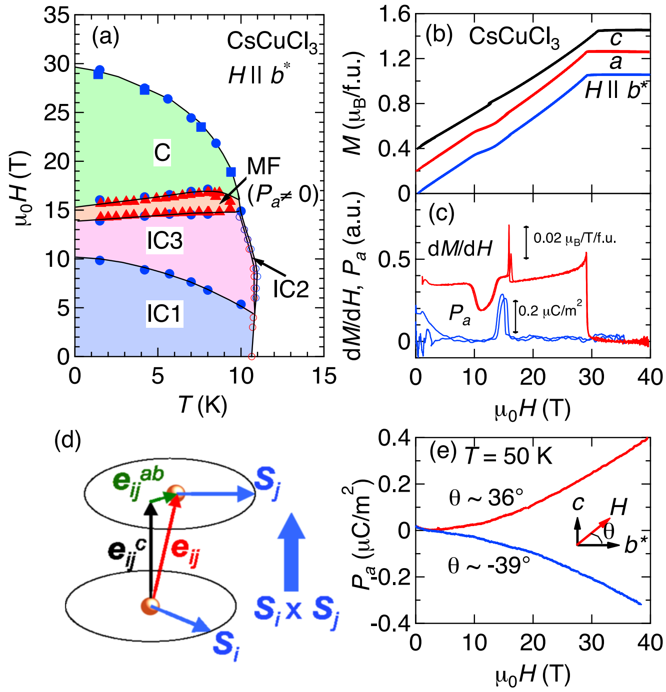

Fig. 1. (a) Magnetoelectric phase diagram of CsCuCl$_3$ in the H_{b^*}-T plane. (b) Magnetic field (H) dependence of magnetization (M) of CsCuCl$_3$ for H parallel to the *a*, *b**, and *c* axes at 1.4 K. (c) H dependence of dM/dH and electric polarization along the *a* axis, P_a, of CsCuCl$_3$ for $H // b^*$ at 1.4 K. (d) Schematic of the two nearest interlayer Cu ions (spheres). Two adjacent spins $\boldsymbol{S}_i$ and $\boldsymbol{S}_j$ are connected with a unit vector $\boldsymbol{e}_{ij}$. (e) $P_a(H)$ curves for the H angle $\theta \sim -39°$ and ~ 36° in the paramagnetic region $T = 50$ K.

between the spin helices (solitons) becomes extremely large, and as a result, a small perturbation like magnetoelectric effects of the second order may align the local electric polarization to one direction. This second order effect, which is called as a paramagnetoelectric effect, is actually resolved by our accurate high-field experiments of the magnetoelectric effects in the paramagnetic phase as shown in Fig. 1(e). The emergence of electric polarization is thus explained by the cooperation of the local electric polarization on the chiral solitonic spin arrangement and the paramagnetoelectric effect. Therefore, we interpret this MF phase in $CsCuCl_3$ as the polar solitonic phase [4].

References

[1] K. Adachi *et al.*, J. Phys. Soc. Jpn. **49**, 545 (1980).
[2] H. Nojiri *et al.*, J. Phys. (Paris) **49**, C8-1459 (1988).
[3] H. Nojiri *et al.*, Physica B **241-243**, 210 (1998).
[4] A. Miyake *et al.*, Phys. Rev. B **92**, 100406(R) (2015).
[5] A. E. Jacobs *et al.*, J. Phys. Soc. Jpn. **62**, 4066 (1993).
[6] N. Stüβer *et al.*, Physica B **350**, e47 (2004).
[7] Y. Togawa *et al.*, Phys. Rev. Lett. **108**, 107202 (2012).

Authors
A. Miyake, J. Shibuya, M. Akaki[a], H. Tanaka[b] and M. Tokunaga
[a]The University of Tokyo and Osaka University
[b]Tokyo Institute of Technology

Novel Spin State Ordering in $LaCoO_3$ Discovered at above 100 T

Y. H. Matsuda and Kindo Groups

In transition metal oxides (TMO), various exotic phenomena emerge such as superconductivity, colossal magnetoresistance, metal-insulator transition, multiferroics and so forth. All these phenomena are considered to originate in the electron correlation that gives rise to the quantum many body effects. Then, the emergent orders appear due to the coupling of multiple degrees of freedom in solids such as spin, charge, lattice. Among TMO, cobaltites are regarded unique for their spin state degree of freedom. For example in the case of the most intensively studied $LaCoO_3$, the electronic state of the trivalent cobalt ion ($3d^6$) is classified into low spin (LS), intermediate spin (IS) and high spin (HS) state according to the total spin angular momentum $S = 0, 1, 2$, respectively, based on the single ion picture.

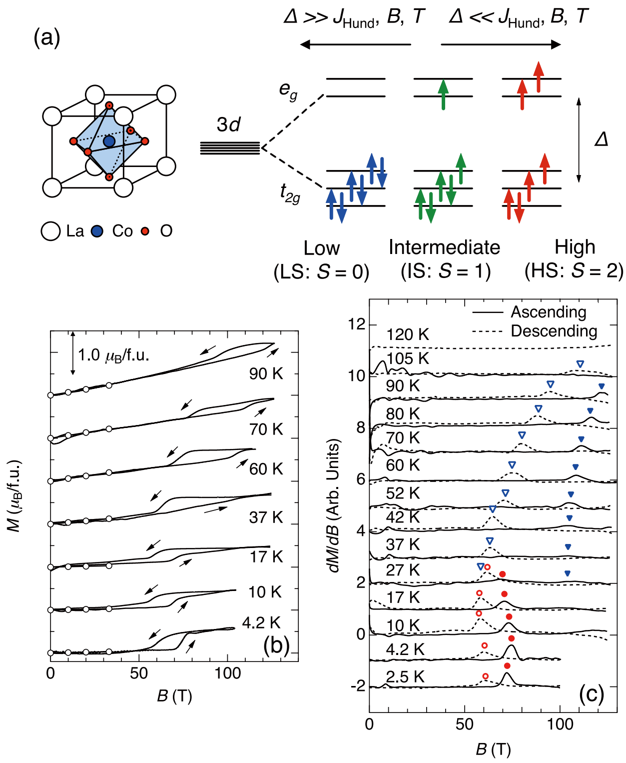

Fig. 1. (a) Schematic drawing of the perovskite structure and electronic configurations of spin state of $LaCoO_3$ (b) Magnetization (M) and (c) dM/dB curves of $LaCoO_3$ measured using induction method up to 130 T generated with the single turn coil method.

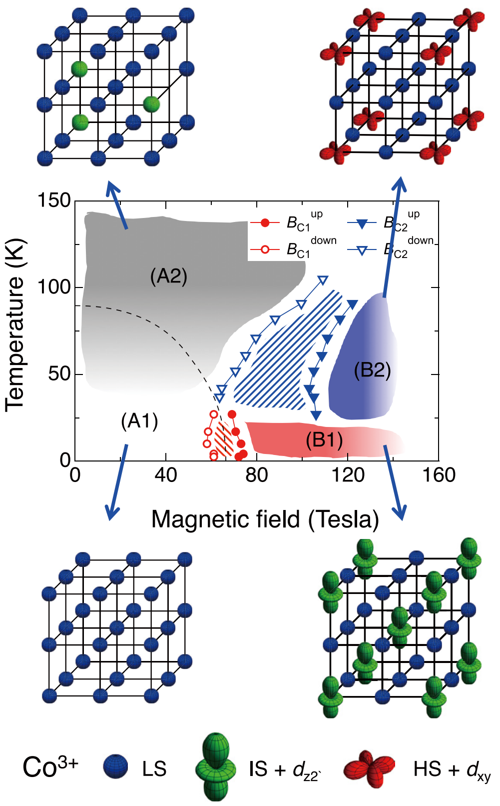

Fig. 2. (a) Magnetic field – Temperature phase diagram of $LaCoO_3$ determined by the magnetization measurements. (b) Tentatively proposed configurations of the spatial ordering of the spin state and orbitals in $LaCoO_3$.

One of the most interesting phenomena expected in cobaltites is the ordering of spin states, which is, however, not observed in general except for the limited cases such as thin films or special materials. Actually, in the case of $LaCoO_3$, no order of spin state has been found for more than half a century. $LaCoO_3$ undergoes the anomalous change in the magnetic and electric properties in the thermal evolution. In fact, even what kind of spin states are involved is still a major matter of debate.

Recently, it becomes clear that high magnetic fields can be used to directly observe the magnetic excited state of $LaCoO_3$. At ISSP UTokyo in 2009, the magnetization jump of 0.5 μ_B/Co at about 60 T was found [1]. At Los Alamos High field laboratory in 2012, another magnetization jump at 70 T was found by measurements up to 100 T [2]. It has been proposed that the spatial ordering of different spin state called spin state crystalline (SSC) phase is realized at high magnetic fields. However, for the confirmation of the SSC, the study up to even more high temperature and high magnetic fields is needed.

In Fig. 1 (b) and (c), we present the measured magnetization (M) and dM/dB up to 130 T and up to 110 K. We found an obviously new magnetic phase at above 100 T and at above 35 K along with the previously found phase of above

65 T and below 35 K in Fig. 2 (a) [3]. We at this moment are considering the origin of the novel phase as follows. At the phase (A1), all Co ions are in LS state. With increasing temperature at the phase (A2), thermally induced IS or HS of Co ions appears with spatially disordered manner. With increasing magnetic field, the phase transition from (A2) to (B2) takes place accompanied with the sudden increase of the number of IS or HS species and also accompanied by the formation of the spatial ordering or IS or HS and LS species, namely, the SSC. In (B2), further order such as orbitals may also be possible on the background of the SSC. With decreasing temperature, another phase transition takes place between (B2) and (B1) without changing the magnetization. At this moment, it is difficult to clarify what is happening in the phase transition between (B1) and (B2). We note that the representative possibilities are the order-disorder phase transition of orbitals, the switching between the different orbital order, the switching between the different SSC. Tentative schematics of such spin state and orbital order are depicted in Fig. 2 (b).

Actually, the origin of the discovered high field phases (B1) and (B2) in $LaCoO_3$ is still an open question. Besides the possibilities mentioned above, the possibilities of the field induced excitonic condensate and the SSC are investigated very recently with the calculations based on the dynamical mean field theory motivated by the present result [4,5]. For further investigation of the origins of the phase (B1) and (B2), different kind of experimental efforts such as the magnetostriction, magnetoresistance, x-ray diffraction at even higher magnetic fields, and the exploration of family materials are quite in demand.

References

[1] K. Sato, A. Matsuo, K. Kindo, Y. Kobayashi, and K. Asai, J. Phys. Soc. Jpn. **78**, 093702 (2009).
[2] M. M. Altarawneh, G. W. Chern, N. Harrison, C. D. Batista, A. Uchida, M. Jaime, D. G. Rickel, S. A. Crooker, C. H. Mielke, J. B. Betts, J. F. Mitchell, and M. J. R. Hoch, Phys. Rev. Lett. **109**, 037201 (2012).
[3] A. Ikeda, T. Nomura, Y. H. Matsuda, A. Matsuo, K. Kindo and K. Sato, Phys. Rev. B **93**, 220401(R) (2016).
[4] A. Sotnikov and J. Kunes, arXiv:1604.01997.
[5] T. Tatsuno, E. Mizoguchi, J. Nasu, M. Naka, and S. Ishihara, arXiv:1606.01681.

Authors
A. Ikeda, T. Nomura, Y. H. Matsuda, A. Matsuo, K. Kindo and K. Sato[a]
[a]Ibaraki National College of Technology

High-Resolution Three-Dimensional Spin- and Angle-Resolved Photoelectron Spectrometer Using Vacuum Ultraviolet Laser Light

Komori and Shin Groups

Spin-polarized electrons in solids have been intensively studied not only for fundamental scientific interests but also for technological applications such as to spintronic devices utilizing the spin degree of freedom. Recently, highly spin-polarized surface states have been discovered under the topological concepts associated with the electronic band structure of materials with strong spin-orbit interaction. Spin- and angle-resolved photoelectron spectroscopy (SARPES) is a powerful technique for investigating such spin-dependent electronic bands. We have constructed a SARPES apparatus [1] with high energy (1.7 meV) and angle resolutions (0.7°) by combining a very-low-energy-electron-diffraction-type (VLEED) spin detector using the oxygen-adsorbed Fe surface [2] and a high-photon-flux vacuum-ultraviolet (VUV) laser, the 6th harmonic of a basic wave of $Nd:YVO_4$ quasi-continuous wave laser with a non-linear optical crystal KBe_2BOF_2. (hν = 6.994 eV) [3]. The spectrometer consists of a hemispherical photoelectron analyzer equipped with a photoelectron deflector function and twin VLEED detectors, as shown in Fig. 1. The latter allows us to analyze the spin vector of a photoelectron three-dimensionally.

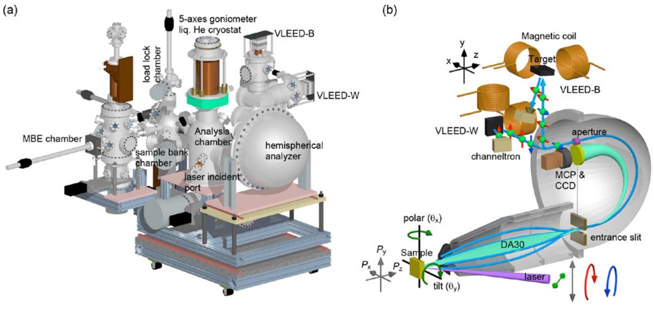

Fig. 1. (a) Overview of the laser-SARPES system developed at the Laser and Synchrotron Research Laboratory. [1] (b) Schematic drawing of the photoelectron detection part of laser-SARPES. The angle between the laser and the analyzer is fixed at 50°. Twin VLEED spin detectors arranged with orthogonal geometry are connected to the hemispherical photoelectron analyzer. The spectrometer is also equipped with electron deflectors at the multi-electron-lens part between the sample and the entrance slit.

We have shown that the present laser-SARPES machine realizes a quick SARPES on the spin-split surface band structure of a Bi(111) film even with 7 meV energy and 0.7° angular resolutions. Figure 2 demonstrates three-dimensional detection of the spin polarization on the Bi(111) surface. We performed three-dimensional SARPES at a point between Γ and K where we can expect non-zero spin polarizations in the x, y, and z directions because of the absence of mirror symmetry on the ΓK line of the Bi(111) surface. In Figs. 2(a)-(f), two spin-polarized surface states, labeled S_1 and S_2, are clearly seen, and the amplitude of the spin vector is summarized in Fig. 2(g). From the spin polarization analysis, we can draw the energy dependence of the spin vector as in Fig. 2(h).

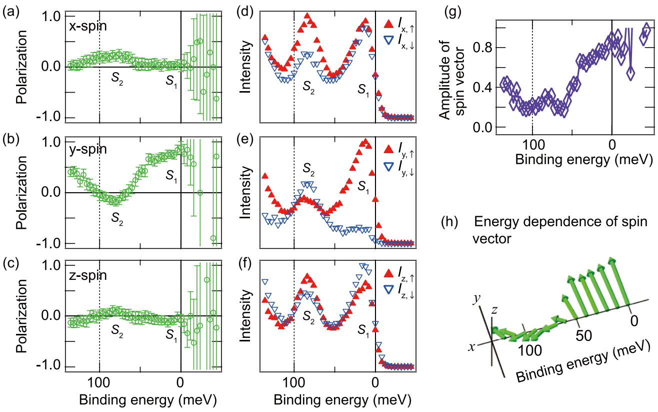

Fig. 2. Spin-polarized surface bands at a point between Γ and K on the Bi(111) surface detected by the three-dimensional laser-SARPES. (a-f) The x (a,d), y (b,e) and z (c,f) components of the spin polarization and the spin-resolved spectra. (g) Amplitude of the spin vector of the photoelectron emitted with the present experimental geometry shown in Fig. 1b. (h) Schematic drawing of the spin vector of the photoelectron emitted from the point between Γ and K as a function of the binding energy. The length of the arrows is proportional to the amplitude of the spin vector.

References
[1] K. Yaji *et. al.*, Rev. Sci. Instrum. **87**, 053111 (2016).
[2] T. Okuda *et. al.*, Rev. Sci. Instrum. **82**, 103302 (2011).
[3] T. Kiss *et. al.*, Rev. Sci. Instrum. **73**, 1875 (2002).

Authors
K. Yaji, A. Harasawa, K. Kuroda, Y. Ishida, A. Fukushima, S. Watanabe[a], C. Chen[b], F. Komori, and S. Shin
[a]Tokyo University of Science
[b]Beijing Center for Crystal Research and Development, Chinese Academy of Science

Ultrafast Spin-Switching of a Ferrimagnetic Alloy at Room Temperature Traced by Resonant Magneto-Optical Kerr Effect Using a Seeded Free Electron Laser

I. Matsuda, Wadati, and Shin Groups

Ultrafast spin dynamics in femtosecond timescale, so-called the femtomagnetism, has been one of the central issues in the frontier science and technology for the last two decades. To capture the nature of the non-equilibrium dynamics, ultrafast time-resolved experiments have been carried out using an ultra- short laser pulses. Recently, the developed EUV-X-ray free electron lasers (FEL) and high harmonic generation (HHG) lasers have opened the opportunity for exploring dynamic phenomena with element selectivity by tuning the photon energy of the laser pulses to the absorption edges of a material. Moreover, since the electron exchange interactions, the most fundamental origin of the magnetism, occur in the femtosecond time-scales, ultrafast experiments using FELs and HHG lasers are expected to add the missing knowledge in condensed matter physics that should bring technological innovation in ultrafast spintronics.

One of the famous ultrafast magnetization phenomena is reversal of GdFeCo ferrimagnetic alloy by optical pumping. GdFeCo is known as a ferrimagnetic metallic alloy, composed of rare-earth (RE) and transition metal (TM) sublattices. The two sublattices couple each other anti-ferromagnetically and spin-switching, induced by a femtoseconds-pulse of either circularly or linearly polarized infrared light, has already been reported. However, there is controversy in the suggested dynamical mechanisms and it was proposed recently that the magnetization reversal process is thermal and the reversal can be explained in terms of the angular momentum conservation when the material is irradiated by circular polarized light. More experimental data, in particular using linearly polarized light, are needed to understand the nature of these opto-magnetic phenomena. In the present study, we extended our resonant magneto-optical Kerr effect (RMOKE) technique for FELs to trace the spin in the Fe (TM) site in a GdFeCo crystal.

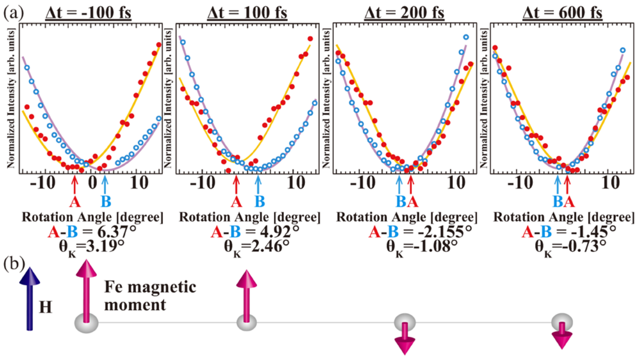

Fig. 1. (a) Experimental results (circles) of the intensity variation with rotation angle taken at hv = 53eV for FEL at each delay time shown in each figure with fitting by cosine curve (solid lines). (b) A schematic diagram of the magnetization reversal dynamics of the Fe magnetic moment with respect to an external field H. The length of the arrows is scaled to the magnitude of the Kerr rotation angle at each delay time shown in (a).

The experiment was performed at FERMI@ELETTRA in Italy by bring our homemade measurement system to the FEL end-station. The Kerr-rotation angle of RMOKE was determined by rotating-analyzer ellipsomtry (RAE) method and time-resolved measurement was carried out by the pump (Ti:S laser) and probe (seeded FEL) technique. Before optical pumping, a sample was set at room temperature, which is above the magnetic compensation temperature of GdFeCo at 250 K and the external magnetic field was applied in the direction of the initial Fe magnetization. Then, the Fe magnetization reversal was traced in *real time* by tuning the photon energy (hv = 53 eV) to the Fe M-absorption edge, which added the element-selectively.

Figure 1(a) shows the results of time-resolved measurements. Each panel shows the RAE results at each indicated delay time. The vertical axis denotes the normalized photon intensity. The two curves (blue and red) correspond to the measurements under the applied magnetic field in up and down direction along the sample surface normal. The solid lines are cosine fitting to the experimental results. The angle zero in each panel corresponds to the extinction state without external field. The Kerr rotation angle at each delay time can be extracted from the phase difference between the two curves. The initial Kerr rotation angle was 3.2 degree at -100 fs (before pumping), which was also measured in the static RMOKE (not shown). Since a polar geometry is used in this TR-RMOKE measurement, the Kerr rotation angle indicates the out-of-plane magnetic moment of Fe in GdFeCo. Figure 1(b) schematically depicts the magnetization dynamics with respect to the external field resulting from the time dependent Kerr rotation angle. The length of the arrows in the figure corresponds to the magnitude of the Kerr rotation angle for each delay time. At 200 fs after the intense laser irradiation, changes of sign of the Kerr rotation angle indicate reversal of Fe magnetization. This reversal mechanism is classified in thermal process, being different from the process involving the inverse Faraday effect in the previous studies using circularly polarized light. Considering the FEL repetition rate of 10 Hz at FERMI@ELETTRA the Fe magnetic moment is recovered at least 100 ms after the pump. Since linearly polarized IR pump laser was used there is no coupling in terms of the exchange of angular momentum between photons and spins in the material. This means that the path for angular momentum transfer is closed between the sub-lattices of Gd and Fe. The timescale of magnetization reversal of TM sublattice is the same as observed in preceding research using time-resolved XMCD, in which transient ferromagnetic-like coupling has been observed due to different demagnetization times for RE and TM sublattices. Our measurement of TR-RMOKE reveals its compatibility with FEL for tracing ultrafast spin dynamics.

References
[1] Sh. Yamamoto *et al.*, Rev. Sci. Instrum. **86**, 083901 (2015).
[2] Sh. Yamamoto *et al.*, Phys. Rev. B **89**, 064423 (2014).

Authors
Sh. Yamamoto, M. Taguchi[a], T. Someya, Y. Kubota, S. Ito, H. Wadati, M. Fujisawa, F. Capotondi[b], E. Pedersoli[b], M. Manfredda[b],

L. Raimondi[b], Maya Kiskinova[b, c], J. Fujii[d], P. Moras[d], T. Tsuyama, T. Nakamura[e], T. Kato[f], T. Higashide[f], S. Iwata[f], S. Yamamoto, S. Shin, and I. Matsuda
[a]Nara Institute of Science and Technology
[b]Elettra-Sincrotrone Trieste
[c]Dipartimento di Fisica, Universita' degli Studi di Trieste
[d]Istituto Officina dei Materiali, Consiglio Nazionale delle Ricerche
[e]Japan Synchrotron Radiation Research Institute/SPring-8
[f]Nagoya University

Optically Detecting Edge-State of Topological Insulator under the Ambient Condition by Ultrafast Infrared Photoluminescence Spectroscopy

Suemoto and I. Matsuda Groups

Three-dimensional topological insulators (TIs) are materials characterized by insulating bulk bands and metallic surface states resulting from a nontrivial topology of the bulk wave functions. The surface states form a Dirac cone structure with electron spins locked perpendicular to their momenta within the bulk band gap. The helical spin structure, which suppresses electron backscattering induced by nonmagnetic impurities, proposes electronic and spintronic device applications of TIs. The robustness of topologically protected surface states under exposure to air furthermore offers to realize versatile TI devices operating under the ambient environment. It is therefore crucial for the device applications to investigate dynamical properties of surface carriers in TIs particularly under the ambient condition. Recently the surface carrier dynamics has been explored with ultrafast time-resolved techniques allowing for distinguishing the bulk and surface response, involving time- and angle-resolved photoemission spectroscopy (TrARPES), optical pump mid-infrared probe spectroscopy (OPMP), and optical pump THz probe spectroscopy (OPTP). TrARPES has been utilized to observe directly the transient electron population with the high momentum and energy resolution, providing knowledge about the electron-phonon scattering and the bulk-surface interband transition in TIs. TrARPES, however, needs the ultra-high vacuum condition to prevent the surface contamination of samples due to the surface sensitivity. In contrast, OPMP and OPTP have delivered insights into the low-energy electronic transition in the surface Dirac cone even under the atmospheric condition with larger penetration depth than that in TrARPES experiments, while being incapable of direct access to excited states over a wide energy range from the surface states to the bulk bands.

Time-resolved photoluminescence spectroscopy (TrLS) overcomes their drawbacks with the bulk sensitivity and the wide-range detection of excited states in visible to infrared regions. TrLS combined with time-resolved photoemission spectroscopy (TrPES) has been applied to graphite, providing deep understanding on the carrier dynamics in the Dirac cone [1]. TrLS is therefore urgently expected to be a practical approach even to surface carrier transitions in TIs under the ambient consition; however, no TI research with TrLS has been reported. Here, we report an application of the infrared TrLS technique to a TI $TlBiSe_2$ under the ambient condition (inset in Fig.1).

A TI $TlBiSe_2$ is known to feature the Dirac point located near the middle point of the bulk band gap of 0.35 eV at the $\bar{\Gamma}$ point, which is a large value among TIs. We used $Tl_{1-x}Bi_{1+x}Se_2$ ($x = 0.025$) synthesized by the Bridgman method as the sample, where the Fermi-level is located near the Dirac point. The infrared time-resolved luminescence measurement was performed with the up-conversion technique under the ambient condition. The $TlBiSe_2$ sample was excited by 70 fs pulses at a wavelength of 800 nm (1.55 eV) from Ti:sapphire regenerative amplifier operating at a repetition rate of 200 kHz. The spot size on the sample was approximately 300 μm in diameter and the fluence was estimated to be 0.34 mJ/cm^2. The visible light was generated by sum-frequency mixing of the infrared luminescence light and the gating pulses at 1.55 eV in an optical nonlinear crystal $LiIO_3$, and detected by a photomultiplier tube coupled with a double grating monochromator. The time resolution estimated by autocorrelation of the pump pulse reflected by the sample and the gating pulse was 168 fs. The energy resolution was approximately 70 meV. The up-conversion measuring system had sensitivity for the luminescence photons between 0.23 eV and 1.3 eV. The spectral sensitivity of the system was calibrated by using the sum-frequency signal between the light from a tungsten lamp with a sapphire window and the gating pulses at 1.55 eV.

Figure 1 shows time evolution curves of the luminescence intensities from the $TlBiSe_2$ crystal at emission photon energy ranging from 0.25 eV to 1.0 eV under the 1.55 eV-photoexcitation. The decay profiles exhibit specifically different shapes with the photon energy. As photon energy decreases from 1.0 eV, the peak position time becomes longer with decrease of the photon energy. This behaviour can be explained in terms of the bulk insulating property: the carriers are accumulated at the bottom of the

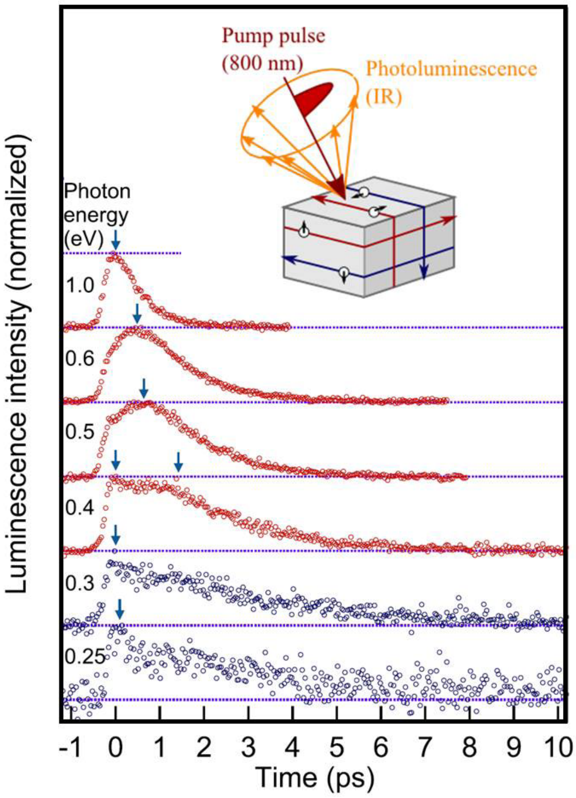

Fig. 1. Time evolution curves of the luminescence intensities from $TlBiSe_2$ at emission photon energy ranging from 0.25 eV to 1.0 eV under 1.55 eV-photoexcitation. The curves are normalized at their own maxima and offset for clarity of display. The curves at lower photon energy than bulk band gap of 0.35 eV are shown in blue. The green arrows indicate the peak position of each curve. The inset shows schematic drawing of the infrared photoluminescence measurement under 1.55 eV (800 nm) pulse excitation.

bulk bands due to the energy band gap, which obstructs phonon-mediated recombination between electrons and holes. The longer decay time at lower photon energy is attributed to slower relaxation of the carrier population at lower energy, reflecting the cooling dynamics of the carriers *via* carrier-phonon interactions. On the other hand, when the photon energy is lower than the bulk band gap of 0.35eV, distinctive decay profiles with much longer decay times (approximately 4 ps) are found at 0.25 eV and 0.3 eV. The decay profile at 0.4 eV, which corresponds to the turning point of the shape change of the decay profiles, consists of two components similar to each decay profile at 0.3 eV and 0.5 eV.

The distinctive shape change of the luminescence decay profiles and the bimodality of the time-resolved luminescence spectra elucidate that the luminescence originates from different energy bands. According to the band calculations, no bulk state resides in the energy band gap region less than 0.6 eV, except each one around the $\overline{\Gamma}$ point (0.35 eV) and the $\overline{\text{M}}$ point (0.3 eV)[2]. The bulk band around the $\overline{\text{M}}$ point might contribute to the luminescence at photon energy even below the bulk band gap of 0.35 eV; however, the decay profile at the photon energy of 0.3 eV that matches the energy band gap at the $\overline{\text{M}}$ point does not exhibit a rapid rise expected from the bulk insulating property[3]. The decay profiles at the photon energy below the bulk band gap of 0.35 eV are therefore attributed to the luminescence predominantly derived from the surface states. The quantitative analyses, based on the rate-equation model, also confirmed this assignment [3].

The topologically protected surface states were optically detected even under the ambient condition, and the relaxation rate of the surface carriers was determined, distinguished from the bulk contribution simply with the emission photon energy. Our results present the availability of the infrared TrLS technique as a novel approach to the dynamical properties of the surface carriers in TIs toward their application to electronic and spintronic devices operating under the ambient environment.

References

[1] T. Suemoto *et al*., Phys. Rev. B **87**, 224302 (2013).
[2] K. Kuroda *et al*., Phys. Rev. Lett. **105**,146801 (2010).
[3] S. Maezawa *et al*., Sci. Rep. **5**, 16443 (2015).

Authors

S. Maezawa, H. Watanabe, M. Takeda, T. Someya, K. Kuroda, I. Matsuda, and T. Suemoto

Development of Sub-300 fs, 100-W Class, Yb-Fiber Based CPA Laser System at 1-MHz

Kobayashi Group

High repetition rate (>MHz) high harmonics generation (HHG) based vacuum ultraviolet (VUV) laser source is highly desirable for photoelectron spectroscopy, for space-charge-free measurement by limiting the number of emitted electrons per pulse, which can lead to higher signal-to-noise-ratios and achieve high energy resolution. Traditionally, Ti:sapphire laser systems were adopted as the driver, which, however, typically have a repetition rate on the order of a few kilohertz, or hundred kilohertz at the expense of the pulse energy. That is mainly limited by the poor thermal conductivity of the Ti:sapphire crystal itself. Even with the state-of-the-art cryogenic configuration, the average power is limited at a few tens of watts.

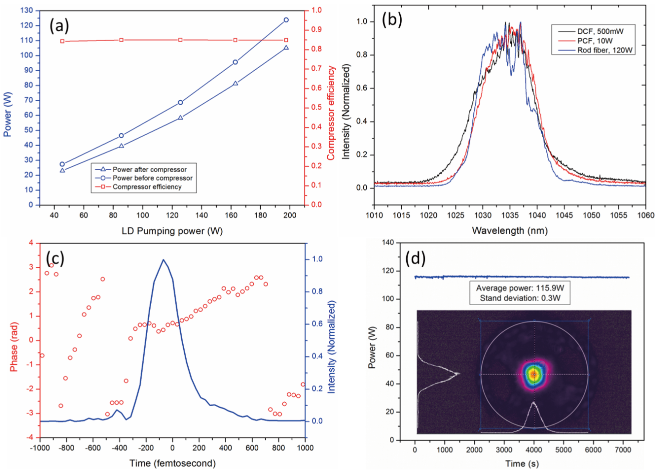

Fig. 1. (a), Power performance of the FCPA system; (b), Spectra taken from different stages of amplification; (c), Pulse intensity and phase obtained from the SHG-FROG measurement; (d), Power stability of the fiber CPA laser system and beam profile.

As far as high repetition rate, high average power lasers are concerned, Yb-based fiber, slab, and disk lasers are leading the trend in this field and all three have enabled >1 kW of average output power, due to their advanced heat dissipating ability. Comparatively speaking, slab lasers and disk lasers give pulse duration on the order of few picosecond or sub-picosecond. While, fiber lasers, due to the broader gain bandwidth they can support, can give shorter pulse duration. Unfavorably, due to the small core diameter of gain fibers, the peak powers reached inside the fiber are high and unwanted nonlinear effects, such as self-phase modulation, tend to occur. Hence, in order to avoid possible nonlinearities, the pulse duration of a seed laser needs to be stretched before it is amplified by a fiber amplifier. Although there have been some reports on high average power 1-MHz fiber chirped pulse amplification (FCPA) lasers, their pulse duration were limited to ~500 fs.

Here we report on a FCPA laser system, which delivered 100 W of output power after a pulse compressor, at a repetition rate of 1 MHz, corresponding to a pulse energy of 100 μJ. The compressor efficiency was as high as 85% thanks to the special large scale transmission gratings. The pulse duration was measured to be 270 fs using second harmonic generation frequency-resolved optical gating (SHG-FROG) method. To the best of our knowledge, this represents the shortest pulse duration achieved by a hundred-watt-level fiber chirped pulse amplification laser system at few MHz repetition rate, without resorting to any means of post-compression and SLM-based phase compensation. The excellent beam quality was guaranteed by the rod fiber itself and by careful alignment into this fiber to effectively excite the fundamental mode alone.

The FCPA system started from a mode-locked 64-MHz Yb:fiber oscillator with an average power of 5 mW. This seed laser was then directed to a grating based pulse stretcher, and stretched to be ~1 ns. A single mode Yb pre-amplifier followed the stretcher to boost the power up to ~100 mW. An acoustic optical modulator (AOM) was used to lower the repetition rate down to 1 MHz. Meanwhile, the average power was decreased to 0.5 mW. Additional two-stage pre-amplifiers increased the average power to 500 mW, which then seeded the following 40/200 photonic crystal fiber (PCF) amplifier that was pumped in the backward direction by a 25 W laser diode at 976nm. The final stage amplifier was a straight 55 cm rod fiber from NKT Photoncis, pumped by a fiber coupled 350-W laser diode centered at 976 nm. With a seed laser of 13W, more than 120 W average power was extracted when backward pumping at ~200 W was used, shown in Fig.1(a). The optical-to-optical efficiency was in excess of 60%. After compressor, more than 100 W of average power were obtained, corresponding to an efficiency of ~85% for the compressor. Fig.1(b) shows the spectrum taken after different amplifier stages. Only minor gain narrowing effects were visible. Figure 1(c) shows the measured pulse duration of ~270 fs. Figure 1(d) shows 2-hours operation of the system.

In the future, we would like to use this laser system to drive HHG process. By that, high repetition rate VUV laser could be expected soon.

Reference

[1] Z. Zhao and Y. Kobayashi, Appl. Phys. Express. **9**, 012701 (2016).

Authors

Z. Zhao, and Y. Kobayashi

Observation of a Devil's Staircase in the Novel Spin-Valve System $SrCo_6O_{11}$

Wadati Group

Combining different materials in artificial nanostructures is a most important approach to create improved or even completely new electronic functionalities for technological applications. A very prominent example of this is the giant magnetoresistance (GMR), which was first realized by multilayers of alternating nonmagnetic and ferromagnetic metals [1] and which now is an indispensable part of today's information technology. In these GMR systems the electrical resistance is high for an antiparallel alignment of the magnetization in the neighboring magnetic layers, while it is low for a parallel alignment of those magnetizations. For this reason such systems are also referred to as spin valves.

Here we report on a high-resolution resonant soft x-ray scattering (RSXS) study of $SrCo_6O_{11}$ bulk single crystals as a function of temperature (T) and applied magnetic field (H) [2]. $SrCo_6O_{11}$ is a particularly interesting material with intrinsic magnetoresistance. Figure 1 (a) shows the lattice structure, which is believed to realize a GMR multilayer system at the atomic scale [3]. One of the most striking magnetic features of $SrCo_6O_{11}$ observed so far are plateaus in the magnetization as a function of the applied magnetic field along the *c* axis as shown in Fig. 1 (b). These plateaus correspond to 1/3 and 3/3 of the saturated moment and were found to reflect different stackings along *c*, namely, an up-up-up structure for the 3/3 phase and an up-up-down configuration for the 1/3 phase.

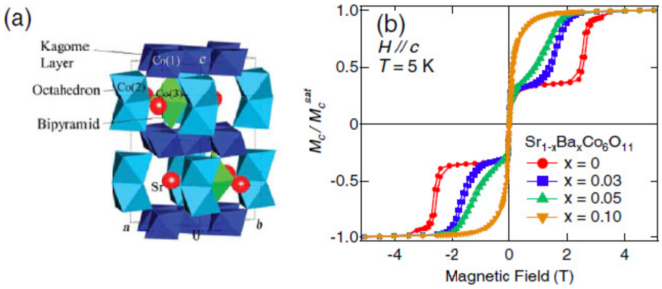

Fig. 1. (a) Crystal structure of $SrCo_6O_{11}$. (b) Out-of-plane magnetization of $Sr_{1-x}Ba_xCo_6O_{11}$ as a function of magnetic field (H // c) at 5 K.

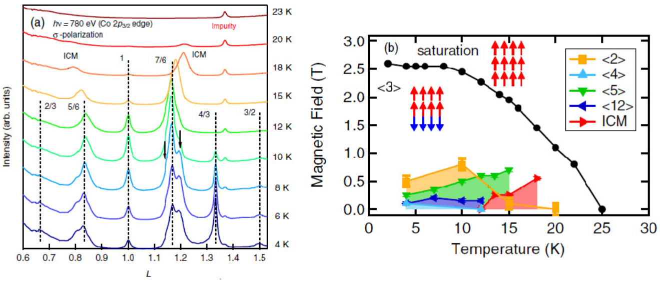

Fig. 2. (a) Magnetic peak profile of $SrCo_6O_{11}$ at various temperatures at zero magnetic field. (b) Magnetic phase diagram of $SrCo_6O_{11}$.

Figure 2 (a) shows the diffraction peaks of $SrCo_6O_{11}$ at zero field for various temperatures. Quite surprisingly and very uncommon for RSXS experiments, a large number of superlattice reflections at L = n/6 with n = 4, 5, 6, 7, 8 and 9 is observed. L = 1 commensurate (CM) peak and two incommensurate (ICM) peaks around L = 0.8, 1.2 appear at 20 K (T_{c1}). These ICM peaks move to L = 5/6 and 7/6, respectively, as the temperature is decreased, and finally are locked at these values at 12 K (T_{c2}), respectively. At T_{c2}, there appear L = 6/5 and 8/7 shoulders of the L = 7/6, and, simultaneously, L = 2/3, 4/3, and 3/2 peaks. These results therefore directly reveal that a large number of magnetic phases coexist in zero magnetic field.

Figure 2 (b) shows the entire H-T diagram of $SrCo_6O_{11}$ determined by RSXS measurements under magnetic fields. Here, <n> represents the magnetic periodicities. The phase diagram demonstrates that various magnetic orderings with different periodicities are formed in the low temperature and low field region. Obviously, the energies of these magnetic structures are quite close, and the corresponding energy differences sensitively depend on temperature and magnetic fields. This phenomenon is called "the devil's staircase," where, in principle, an infinite number of commensurate superstructures can be realized by tuning an external parameter. As these corresponding eigenstates (magnetic orderings in this case) have similar energies, they can be switched from one to another by small perturbation. In this case of magnetic ordering, the mechanism is described by the axial next-nearest-neighboring Ising (ANNNI) model. The ANNNI model describes competing interactions between nearest (J_1) and next-nearest (J_2) Ising spins, which yields various magnetic orderings with close energies in the phase diagram of temperature and J_2/J_1. However, in order to explain ordered structures with long periodicities, one needs magnetic interactions that go well beyond the nearest neighbors. A plausible explanation can be provided by the Ruderman-Kittel-Kasuya-Yosida (RKKY) interaction via the metallic planes.

References

[1] M. N. Baibich, J. M. Broto, A. Fert, F. Nguyen Van Dau, F. Petroff, P. Etienne, G. Creuzet, A. Friederich, and J. Chazelas, Phys. Rev. Lett. **61**, 2472 (1988).
[2] T. Matsuda, S. Partzsch, T. Tsuyama, E. Schierle, E. Weschke, J. Geck, T. Saito, S. Ishiwata, Y. Tokura, and H. Wadati, Phys. Rev. Lett. **114**, 236403 (2015).
[3] S. Ishiwata, I. Terasaki, F. Ishii, N. Nagaosa, H. Mukuda, Y. Kitaoka, T. Saito, and M. Takano, Phys. Rev. Lett. **98**, 217201 (2007).

Authors

T. Matsuda[a], S. Partzsch[b], T. Tsuyama, E. Schierle[c], E. Weschke[c], J. Geck[b], T. Saito[d], S. Ishiwata[a], Y. Tokura[a,e], and H. Wadati

[a]Department of Applied Physics and Quantum-Phase Electronics Center (QPEC), the University of Tokyo
[b]Leibniz Institute for Solid State and Materials Research IFW Dresden
[c]Helmholtz-Zentrum Berlin für Materialien und Energie
[d]Institute for Chemical Research, Kyoto University
[e]RIKEN Center for Emergent Matter Science (CEMS)

Quadratic Fermi Node in a 3D Strongly Correlated Semimetal

Kondo, Nakatsuji, and Shin Groups

Strong spin–orbit coupling fosters exotic electronic states such as topological insulators and superconductors, but the combination of strong spin–orbit and strong electron–electron interactions is just beginning to be understood. Central to this emerging area are the 5*d* transition metal iridium oxides [1-4]. Here, in the pyrochlore iridate $Pr_2Ir_2O_7$, we identify a non-trivial state with a single-point Fermi node protected by cubic and time-reversal symmetries, using a combination of angle-resolved photoemission spectroscopy and first-principles calculations. Owing to its quadratic dispersion, the unique coincidence of four degenerate states at the Fermi energy, and strong Coulomb interactions, non-Fermi liquid behavior is predicted, for which we observe some evidence. Our discovery implies that $Pr_2Ir_2O_7$ is a parent state that can be manipulated to produce other strongly correlated topological phases, such as topological Mott insulator, Weyl semimetal, and quantum spin and anomalous Hall states.

The experimental evidence for a quadratic Fermi node state in $Pr_2Ir_2O_7$ is demonstrated in Fig. 2. In the panel (d), we observe that a parabolic energy-dispersion approaches E_F with increasing photon energies (or k_z values), and finally touches it at the Γ point (a red curve). We have confirmed that, with further increase of k_z, the dispersion gets away from E_F again, which signifies that the 3D band structure of $Pr_2Ir_2O_7$ has a single Fermi point (Fig. 2(b)). Other scans of different k_z values up to the L point (Fig.(c)) revealed no other states touching or crossing E_F. This circumstance satisfies the charge neutrality, and it could be a further evidence for the realization of nodal state. We also find that the broad spectral weight emerges beyond E_F as seen in the Fermi-function-divided image for the 75K data (arrow in Fig. 2(e)). This observation is compatible with the predicted existence of a quadratic band touching on the unoccupied side.

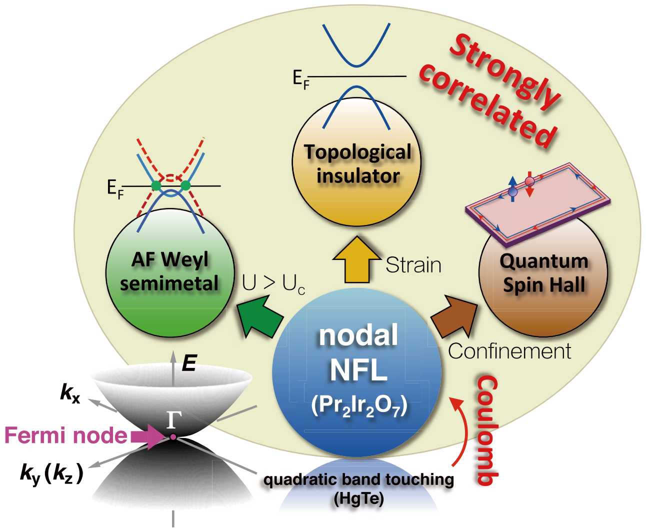

Fig. 1. Quadratic Fermi node state of $Pr_2Ir_2O_7$ tunable into interacting topological phases. In the lower part of the diagram, the bottom half of the blue circle and its reflection form a caricature of the quadratically dispersion conduction and valence bands touching at the zone centre, while at the same time the darker-blue upper circle suggests how $Pr_2Ir_2O_7$, with non-negligible Coulomb interactions, is a strongly correlated non-Fermi liquid analogue of HgTe, shown as a pale-blue reflection. Arrows indicate the perturbations that convert the nodal non-Fermi liquid state to diverse topological phases.

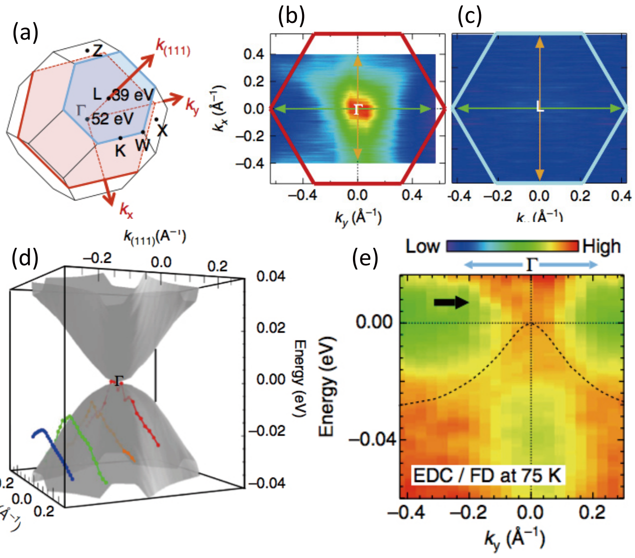

Fig. 2. Fermi node state of $Pr_2Ir_2O_7$ revealed by ARPES with synchrotron radiation source. (**a**) Brillouin zone, showing measured momentum sheets. (**b,c**) ARPES intensities at E_F in the k_x-k_y sheet crossing Γ and L measured at *hν*=52eV and 39eV, respectively. The calculated band dispersion in the k_x-$k_{(111)}$ sheet. Energy dispersions determined by ARPES are plotted on it. (**e**) ARPES dispersion map crossing Γ, measured at an elevated temperature (*T*=75K).

References

[1] B. J. Kim *et al.*, Science **323**, 1329 (2009).
[2] Y. Machida *et al.*, Nature **463**, 210 (2009).
[3] D. Pesin *et al.*, Nature Physics **6**, 376 (2010).
[4] X. Wan *et al.*, Phys. Rev. B **83**, 205101 (2011).
[5] T. Kondo *et al.*, Nature communications **6**, 10042 (2015).

Authors

T. Kondo, M. Nakayama, R. Chen[a], J. J. Ishikawa, E.-G. Moon[a], T. Yamamoto, Y. Ota, W. Malaeb, H. Kanai, Y. Nakashima, Y. Ishida, R. Yoshida, H. Yamamoto, M. Matsunami[b], S. Kimura[b], N. Inami[c], K. Ono[c], H. Kumigashira[c], S. Nakatsuji, L. Balents[a] , and S. Shin
[a]University of California
[b]UVSOR Facility, Institute for Molecular Science
[c]High Energy Accelerator Research Organization (KEK)